GEOLOGICA CARPATHICA, 2025, 76, 3, 189–208 https://doi.org/10.31577/GeolCarp.2025.10

"Dry" and "wet" alteration of magmatic monazite in Variscan crystalline rocks from Mt. Papuk (Croatia)

ETIENNE SKRZYPEK[1,✉], DANIELA GALLHOFER[1], DRAŽEN BALEN[2], PETRA SCHNEIDER[2] and CHRISTOPH A. HAUZENBERGER[1]

[1]Department of Petrology and Geochemistry, NAWI Graz Geocenter, University of Graz, Universitätsplatz 2, 8010 Graz, Austria
[2]Department of Geology, Faculty of Science, University of Zagreb, Horvatovac 102a, 10000 Zagreb, Croatia

(Manuscript received May 4, 2025; accepted in revised form July 14, 2025; Associate Editor: Milan Kohút)

Abstract: Monazite is a valuable geochronometer but is highly prone to react after its formation. Its alteration reactions must therefore be understood to assess its geochronological potential as well as the mobility of rare earth elements and actinides. We study contrasting monazite alteration textures in two different lithologies from Mt. Papuk (Slavonian Mts., Croatia) in order to constrain the timing of thermal events in this eastern exposure of the European Variscan belt, and explore the role of fluids and host-rock composition during monazite alteration. For a migmatite and peraluminous granite sample, we document the texture and composition of monazite-(Ce) and associated phases (xenotime-(Y), actinide-rich phases) and date them by EPMA and/or LA-ICP-MS. The texture observed in the quartz–feldspar±biotite migmatite (Trešnjevica) shows a replacement of primary magmatic monazite by secondary (Th-poorer and LREE-richer) monazite, xenotime and Th–Si-rich phases, and is locally rimmed by apatite. The re-integrated composition of this texture is compatible with that of (Th- and Y-richer) primary monazite. Primary monazite domains yield a magmatic crystallization age of 351±9 Ma while secondary domains are contaminated by initial Pb or give slightly younger Th–U–total Pb and $^{208}Pb/^{232}Th$ dates (~340 Ma). The texture found in the two-mica granite (Zvečevo) involves replacement by apatite and allanite, with some secondary (Th-poorer) monazite and minute uraninite or Th–Si-rich phases. Relicts of primary monazite grains record magmatic crystallization at 352±9 Ma, like primary xenotime domains. Secondary monazite contains initial Pb, secondary xenotime domains yield $^{206}Pb/^{238}U$ dates younger than 338 Ma and uraninite preserves Th–U–total Pb dates averaging at 332 Ma. The first texture indicates a "dry" decomposition that lacks evidence for the mediation of a fluid phase and efficiently trapped all elements (except Y) at the location of the monazite precursor. It is attributed to monazite re-equilibration (Th and Y+HREE loss) at subsolidus conditions. The second texture points to a "wet" replacement by hydrous minerals that needs the presence of fluid and led to REE mobility at least at the millimetre scale. The contrast between both reactions is ascribed to sample composition, one being an anhydrous migmatite hardly affected by fluid infiltration and the other offering all necessary components for Ca and H_2O mobility. Both alteration reactions are correlated with a late Variscan thermal event at ca. 335 Ma. The latter could also be dated using actinide-rich phases, in which case tiny U-oxides appear more reliable than Th-silicates.

Keywords: monazite-(Ce), xenotime-(Y), uraninite, U–Th dating, Slavonian Mountains, European Variscan belt

Introduction

Monazite is an accessory, rare-earth-element- (REE) and commonly actinide-bearing phosphate that is widely used for petrological (e.g., Heinrich et al. 1997; Stepanov et al. 2012) and geochronological (e.g., Harrison et al. 2002; Montel et al. 2018) purposes. It originally grows from a crystallizing magma or at pressure–temperature (*P–T*) conditions ranging from diagenesis to anatexis (e.g., Evans et al. 2002; Goncalves et al. 2004), but an extensive body of natural and experimental studies rather emphasizes its propensity to react (e.g., Oelkers & Poitrasson 2002; Berger et al. 2008; Harlov & Hetherington 2010; Williams et al. 2011). This high reactivity leads to an alteration of its original shape, composition and isotopic record (e.g., Seydoux-Guillaume et al. 2002), so that the central issue is not whether primary monazite will eventually be altered or not, but how and when.

How does monazite alter? Several workers have proposed chemical reactions responsible for monazite replacement or recrystallization (e.g., Broska & Siman 1998; Broska et al. 2005; Krenn et al. 2012; Budzyń et al. 2020). They generally involve REE- and actinide-bearing phases (allanite, thorite), phosphates (apatite, xenotime) or carbonates (bastnäsite, synchisite) together with a fluid phase (e.g., Förster 2001; Bosse et al. 2009; Harlov et al. 2020). The role of the latter was investigated in numerous studies that identify alkali- or fluorine-bearing fluids as the most efficient to alter monazite (e.g., Harlov et al. 2011; Didier et al. 2013). It is, however, not always clear where the fluids come from, how much is needed, and if alteration reactions are isochemical. These aspects have implications for the mobility of REE and actinides (e.g., Jefferies 1985), which is crucial not only for the formation of potential ore deposits (e.g., Harlov et al. 2016) but also regarding the robustness of monazite-like matrices for radioactive waste storage (e.g., Poitrasson et al. 2000).

When does monazite alter? It apparently does not need long to react, as shown by examples of monazite alteration already

✉ corresponding author: Etienne Skrzypek
etienne.skrzypek@uni-graz.at

during magmatic crystallization (Dini et al. 2004) or shortly after (e.g., Broska et al. 2024). It can of course react tens of million years after its formation as a response to low- (e.g., Townsend et al. 2001) or high-grade metamorphic overprints (e.g., Be Mezeme et al. 2006). In all cases the reactions reflect a change in the local bulk composition and/or *P–T* conditions (e.g., Janots et al. 2008), which highlights the potential to date various tectono-thermal events (e.g., Mahan et al. 2006; Mottram et al. 2015). For that purpose, isotopic dating methods should be used in combination with a petrological characterization of alteration textures (e.g., Catlos 2013; Engi 2017).

Lithologies in which monazite formed from a crystallizing melt are arguably best suited to study monazite alteration (e.g., Poitrasson et al. 1996). They commonly preserve primary euhedral grains with rare inclusions and sharp internal zoning patterns that can be easily distinguished from those affected by subsequent alteration (e.g., Skrzypek et al. 2020). Appropriate lithologies are medium- to coarse-grained granitoids or migmatites, which readily allow constraints to be placed on the role of major minerals in alteration processes. For these reasons, we decided to investigate monazite alteration textures in two lithologies – one migmatite and one S-type granite – from Papuk igneous and metamorphic complex in the Slavonian Mountains (Croatia). The main objective is to assess the amount, and possibly the origin, of aqueous fluid involved in monazite alteration. An additional goal is to make use of this accessory mineral, so far rarely considered in crystalline rocks from Mt. Papuk, to gain insights into the timing of tectono-thermal events in this eastern exposure of the European Variscan belt (Fig. 1).

Two localities located less than 10 km apart were selected in crystalline rocks from Mt. Papuk (Fig. 1). The alteration of magmatic monazite is explored in a virtually anhydrous, quartz–feldspar migmatite (Trešnjevica) and a two-mica peraluminous granite (Zvečevo), for which whole-rock and major-mineral compositions are documented. Alteration textures involving primary monazite and other accessory phases are described, and the composition and chemical date of monazite, xenotime and actinide-rich phases has been determined by electron probe micro-analyzer (EPMA). Separated monazite and xenotime grains were additionally dated by laser ablation-inductively coupled plasma-mass spectrometry (LA-ICP-MS). Two different alteration reactions are proposed, and mass balance calculations are used to evaluate their isochemical character, the amount of fluid involved and element mobility. Dating results were finally used to constrain the timing of magmatic monazite crystallization and subsequent alteration.

Geology of Mt. Papuk area (Croatia)

From western to central Europe the Variscan belt exposes voluminous granitoids and related metamorphic rocks in areas such as the Massif Central, Vosges, Black Forest or Bohemian Massif (e.g., Franke 2000). This belt extends eastward to Romania, Bulgaria, Greece and up to Turkey as indicated by small fragments that record pre-Variscan events (Balen et al. 2006, 2015). In northern Croatia, Variscan and pre-Variscan igneous and/or metamorphic events are recognized in crystalline lithologies that crop out in the Slavonian Mountains (Fig. 1). Mt. Papuk occupies the major part of the Slavonian Mountains and lies in the southern part of the Pannonian Basin. There, pre-Alpine lithologies represent surface exposures of the basement of the Pannonian Basin and belong, according to large-scale reconstructions, to the Tisia (Tisija, Tisza) Mega-Unit (e.g., Schmid et al. 2008). The Tisia Mega-Unit comprises southward dipping Alpine nappe systems (Mecsek, Bihor and Codru) that all contain both basement and post-Variscan thrust sequences. Mt. Papuk belongs to the Bihor nappe system and is the largest continuous exposure of pre-Alpine crystalline basement in southern Tisia (e.g., Pamić et al. 2002). This basement is locally covered by Upper Permian to Mesozoic sediments and by the Neogene to Quaternary infill of the Pannonian Basin (Jamičić & Brkić 1987; Jamičić 1989).

The pre-Alpine basement of Mt. Papuk is divided into three complexes (Jamičić 1983; Fig. 1): (1) the Psunj complex (also known as the Kutjevo metamorphic series) is a low- to medium-grade metamorphic complex consisting of chlorite schist, micaschist, paragneiss, amphibolite, metagabbro and marble intruded by granitoids; (2) the Papuk complex (also referred to as the Jankovac metamorphic series) consists of S-type granitic pluton(s) surrounded by medium- to high-grade amphibolite, micaschist and locally migmatitic gneiss; (3) the Radlovac complex consists of very low- to low-grade slate, meta-graywacke, meta-conglomerate and phyllite locally intruded by metabasic rocks. The latter is unconformably covered by a clastic–carbonate sequence from the Upper Permian and Triassic. The first two complexes were combined by Pamić & Lanphere (1991) on the basis of extensive, but mainly K–Ar age dating (Pamić et al. 1988) into a "Progressively metamorphosed complex" (also called "Progressive metamorphic succession" and/or "Prograde metamorphic sequence"), which covers practically the whole of Mt. Papuk.

The Papuk complex (included in the unified "Progressively metamorphosed complex" by Pamić & Lanphere 1991) is interpreted to be the product of Variscan tectono-metamorphic events (Pamić & Lanphere 1991). For metamorphic samples, early studies report K–Ar hornblende dates that mostly lie in the range 376–353 Ma and a Rb–Sr whole-rock result of 317 Ma for amphibolite samples (Pamić et al. 1988). This is supported by dating of monazite in gneissic rocks (374.1±5.8 Ma; Balen & Massonne 2020), granitic pebbles (338±15 Ma; Biševac et al. 2011) and metasediments (330±10 Ma; Biševac et al. 2013) from the Papuk complex as well as in micaschist from the Psunj complex (356±23 Ma; Horváth et al. 2010), while a U–Pb apatite date of 326±23 is ascribed to medium-grade thermal overprinting of a diorite from Mt. Papuk (Balen et al. 2018b). Evidence for Variscan magmatic activity in the Papuk complex comes from age dating of S-type granites and migmatites, with most K–Ar amphibole, biotite and muscovite dates in the range 336–324 Ma and a Rb–Sr whole-rock date of 314 Ma

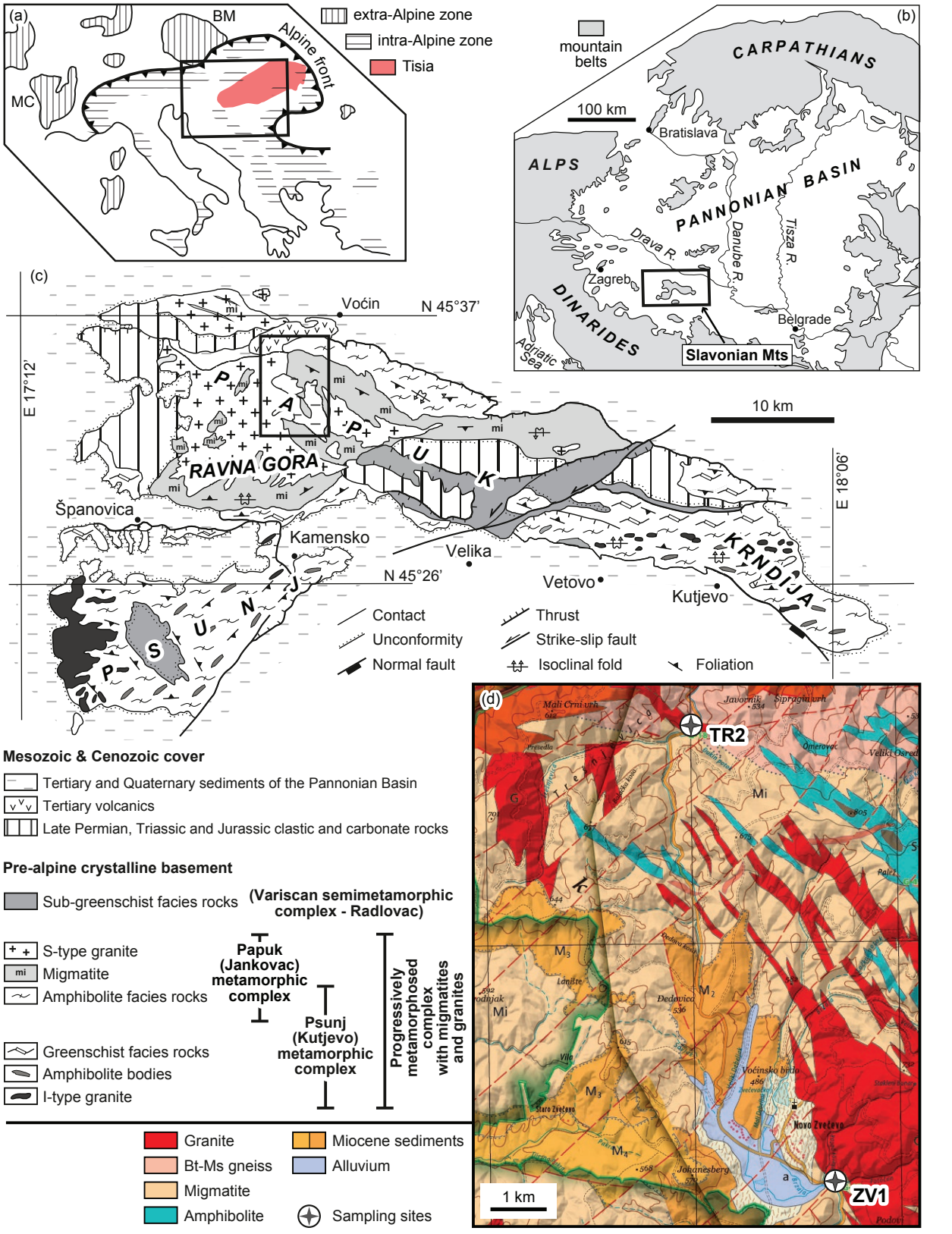

Fig. 1. Geology of Mt. Papuk area, Slavonian Mountains (Croatia). **a** — Position of the Tisia Mega-Unit with respect to Variscan and Alpine systems (BM=Bohemian Massif, MC=Massif Central). **b** — Position of the Slavonian Mts. within the Alpine–Carpathian–Dinarides system. **c** — Schematic geological map of the Slavonian Mts., with pre-Alpine crystalline igneous and metamorphic complexes (modified after Jamičić 1983, 1988, 1989; Jamičić & Brkić 1987; Jamičić et al. 1987, 1989; Pamić & Lanphere 1991). **d** — Geological map of the research area with sample locations (modified geological map after Jamičić & Brkić 1987; Jamičić 1989).

(Pamić et al.1988), and from a U–Pb zircon date of 383±5 Ma obtained for two monzogranite samples (Horvat et al. 2018).

Analytical methods

Sample preparation

Samples from two localities (Trešnjevica – TR2 and Zvečevo – ZV1; Fig. 1d) were selected to prepare several petrographic thin sections. Those were used to document textural relationships and analyze the composition of major minerals and actinide-rich phases. The age and composition of monazite and xenotime were determined on separated grains extracted from ~20 cm^3-sized blocks by crushing, sieving (<400 μm) and panning. For each sample about 50 euhedral to rounded, yellowish monazite grains and a few xenotime grains were handpicked under a binocular microscope and embedded in epoxy resin. Picking, although done randomly, visibly introduced a sampling bias towards less altered monazite grains compared to the proportion observed in thin section.

Whole-rock and mineral compositions

Whole-rock compositions were obtained at the Department of Earth Sciences (NAWI Graz Geocenter, University of Graz) using a Bruker Tiger S8-II X-ray fluorescence spectrometer on lithium tetraborate/metaborate-fluxed glass beads (major elements and selected trace elements). The results are shown in Table 1 together with a mesonorm calculation (after Mielke & Winkler 1979) made using GCDkit (Janoušek et al. 2006).

A JXA-8530FPlus HyperProbe Electron Probe Micro-Analyzer (NAWI Graz Geocenter, University of Graz) equipped with five wavelength-dispersive spectrometers (WDS) was used to determine the composition of major and accessory minerals with a 15 kV acceleration voltage. Beam current and spot diameter conditions were: 10 nA and 3–5 μm for major minerals, 150 nA and 5 μm for monazite and xenotime, and 50 nA with a focused beam for actinide-rich phases. The position of spot analyses in monazite and xenotime was mainly guided by BSE images, as these commonly show a clear difference between primary and altered domains. In order to explore differences or similarities between BSE signal and element distribution, X-ray maps of selected grains were acquired at 100 nA with a focused beam (0.76 μm pixel size) and 45 ms dwell time. For accessory-mineral analyses, interference corrections for Y on PKα and PbMα, Th on UMα and PbMα, U on PbMβ, Sm and Dy on TmLα, Dy and Ho on LuLα, and Tb on ErLα were applied, and matrix correction followed the method of Bence & Albee (1968) with α-factors after Kato (2005). Background positions for the analyzed X-ray lines were determined by WDS scans around the peaks (±15 mm) on an in-house collection of monazite specimens and actinide-rich phases from the investigated samples. All investigated monazite and xenotime grains are monazite-(Ce) and xenotime-(Y). Elk Mountain (1404−1391 Ma; Peterman et al. 2012), 44069 (424.9±0.4 Ma; Aleinikoff et al. 2006) and Gföhl (340±4 Ma; Friedl et al. 1993) monazites were analyzed to assess the accuracy of Th−U−total Pb dates calculated from EPMA analyses. All indicate less than 3 % accuracy offset (see Supplementary Table S1). The Th−U−total Pb dates obtained for xenotime are only indicative; they have a poor precision due to the relatively large uncertainty on Pb content (~ 25 % on average). The full set of analytical conditions, interference corrections (for accessory minerals) and EPMA analyses with Th−U−Pb data is given as Electronic Supplementary Material (Supplementary Table S1).

U−Pb monazite and xenotime dating by LA-ICP-MS

Isotopic analyses of monazite and xenotime were conducted at the Department of Earth Sciences (NAWI Graz Geocenter, University of Graz) on separated grains. An ESI New Wave 193 Excimer Laser (193 nm wavelength) was used to ablate material for 15 s with a 10 μm spot diameter, 7 Hz frequency and fluence of ~3 J/cm^2. The ablated material was transported to an Agilent 7900 series single-collector quadrupole ICP-MS system, and ^{202}Hg, ^{204}(Hg+Pb), ^{206}Pb, ^{207}Pb, ^{208}Pb, ^{232}Th, and ^{238}U were monitored. Monazite 44069 (Aleinikoff et al. 2006) served as primary reference material while Kibe (99−98 Ma; Skrzypek et al. 2016), Moacyr (~508 Ma; Gonçalves et al. 2016), Madmon (523–496 Ma; Schulz et al. 2007), Weinsberg (~323 Ma; Friedl et al. 1996) and TS-Mnz (~910 Ma; Budzyń et al. 2021) monazites were employed as secondary reference materials. Secondary standard analyses indicate less than 2 % accuracy offset on both ^{206}Pb/^{238}U and ^{208}Pb/^{232}Th dates (see Supplementary Table S2). Data reduction was done with Iolite v. 3.71 (Paton et al. 2010, 2011) using the U−Pb–Geochron4 data reduction scheme. Monazite U–Pb analyses with less than 5 % discordance are referred to as concordant. Diagrams and calculations were done with Isoplot 3.76 (Ludwig 2004).

Table 1: Whole-rock compositions and results of mesorm calculations.

	SiO_2	TiO_2	Al_2O_3	Fe_2O_3	MnO	MgO	CaO	K_2O	Na_2O	P_2O_5	LOI	Sum
TR2	77.13	0.08	12.06	0.57	<0.01	0.16	0.14	5.26	2.97	0.025	0.4	98.93
ZV1	70.84	0.29	14.99	1.93	0.032	0.67	1.49	3.54	4.09	0.176	0.68	98.91
	Or	**Ab**	**An**	**Qtz**	**Bt**	**Am**	**Crn**	**Ap**	**Ilm**		**Rest**	**Sum**
TR2	30.7	25.2	0.5	39.5	0.6	0.0	1.3	0.1	0.1		0.0	97.8
ZV1	19.2	34.6	6.2	30.8	2.6	0.0	2.1	0.4	0.3		−0.1	96.1

Note: All Fe treated as FeO for mesonorm calculation

All reported uncertainties are given at the two standard deviation level (2SD), and final age uncertainties include the contribution of long-term excess variance (~2.5 % with the Agilent 7900 in Graz). The full set of analytical conditions and results is available as Electronic Supplementary Material (Supplementary Table S2).

Sample description

Trešnjevica migmatite – TR2

The abandoned quarry at the locality of Trešnjevica exposes mainly leucocratic gneiss cross-cut by various subvolcanic dykes. The dominant lithology is a medium-grained and well-foliated migmatitic orthogneiss with continuous biotite-rich layers (Fig. 2a). It is cross-cut by subparallel layers (several metres in thickness) and oblique to perpendicular isotropic pockets (dm-sized) or veins (cm wide) of finer-grained, quartz–feldspar leucosomes with minor biotite (Fig. 2a). Sample TR2 [45°35'31"N, 17°30'3"E] is a nebulitic migmatite with an isotropic structure, locally cut by quartz–plagioclase veinlets (Fig. 2b). It shows an equigranular texture with subhedral K-feldspar (with perthite or microcline twinning), subhedral plagioclase and rounded quartz. Minor biotite is strongly chloritized and locally hosts secondary muscovite (Fig. 2c). Accessory minerals consist of zircon, monazite, apatite and xenotime.

Sample TR2 is relatively rich in Si and K (Aluminium Saturation Index=1.1) and contains only little Fe–Mg, which translates into a low amount of normative biotite (0.6 %; Table 1). Alkali feldspar has an orthoclase composition ($Ab_{05}Or_{95}$) with albite exsolution ($Ab_{98}An_{01}Or_{01}$). Plagioclase is zoned from an oligoclase core ($Ab_{84}An_{15}Or_{01}$) to an albite outermost rim ($Ab_{95}An_{03}Or_{02}$). White mica contains almost no phengite component (Si=3.07–3.10 apfu) and little Na (0.04–0.06 apfu), while chlorite has a brunsvigite composition with an average Si of 2.83 apfu and X_{Mg} of 0.25.

Zvečevo granite – ZV1

The Zvečevo granite is exposed in the central part of Mt. Papuk and consists of a medium-grained, two-mica granite with biotite-rich refractory relicts and common aplite veins (Fig. 2d). Sample ZV1 [45°32'20"N, 17°31'21"E; geosite Potočan] is a granite with an isotropic structure and blueish alkali feldspar typical for this lithology (Fig. 2e). It contains K-felsdpar phenocrysts (5 mm in length) with a perthitic

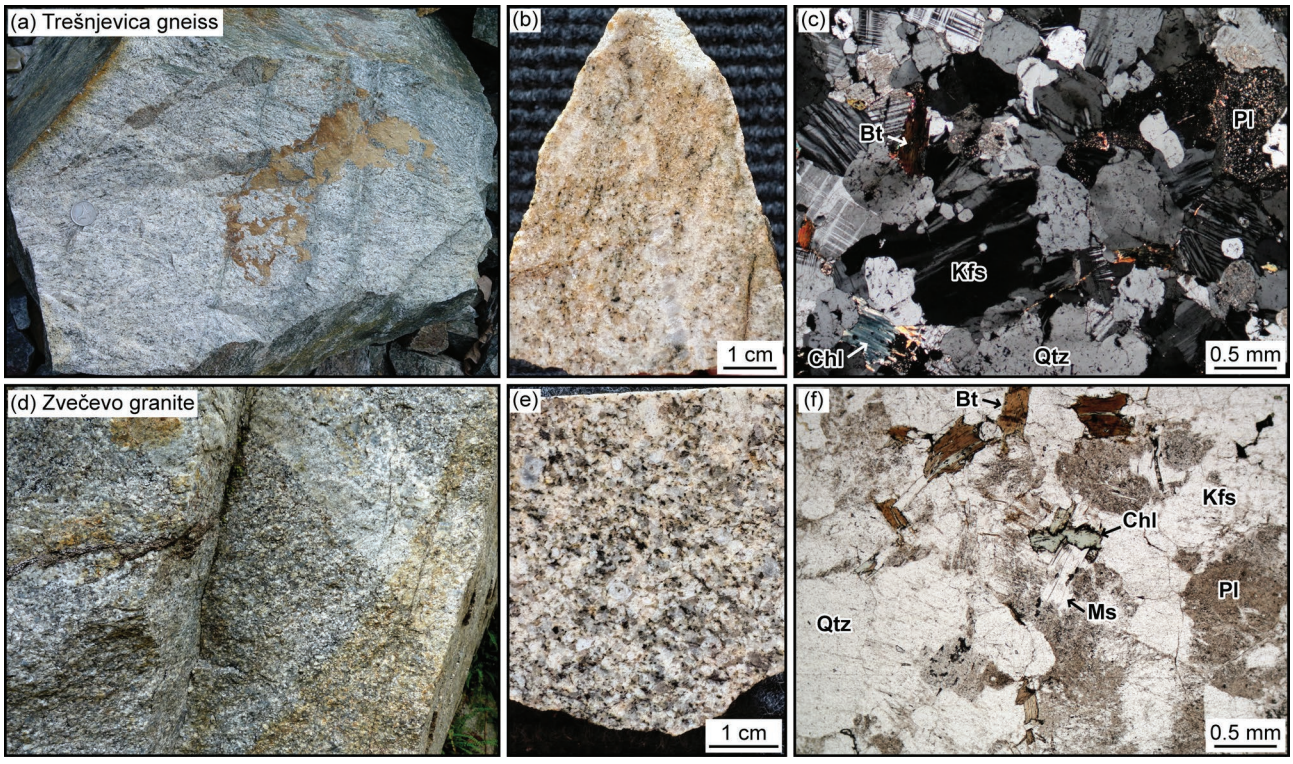

Fig. 2. Photographs of outcrops, hand specimens and thin sections from Trešnjevica gneiss (**a**–**c**) and Zvečevo granite (**d**–**f**). **a** — Gneiss block from Trešnjevica quarry with a pervasive foliation (upper part) grading into a more isotropic, leucocratic domain (lower part) and cut by melanocratic, partly weathered veins. **b** — Nebulitic migmatite cut by a quartz–plagioclase vein. **c** — Granular texture with euhedral feldspar, rounded quartz and rare biotite (crossed polarizers). **d** — Zvečevo granite with biotite-rich patches and cut by an aplite vein (~10 cm in thickness). **e** — Polished slab of medium-grained granite. **f** — Granular texture with large K-feldspar, altered plagioclase, two micas and chlorite (plane-polarized light). Mineral abbreviations follow IUGS recommendations after Kretz (1983).

texture or microcline twinning and locally surrounded by myrmekite, subhedral plagioclase showing sericitization in the core, rounded quartz, muscovite laths and variably chloritized biotite. Accessory phases are zircon, monazite, apatite, allanite and titanite.

Sample ZV1 is a peraluminous granite (Aluminium Saturation Index=1.2) with Na_2O+K_2O=7.63 wt% and Fe_2O_3+MgO=2.6 wt%, in agreement with the common presence of biotite in thin section (2.6 % normative biotite predicted; Table 1). The composition of alkali feldspar is orthoclase ($Ab_{07}Or_{93}$) with albite exsolutions ($Ab_{94}An_{03}Or_{03}$). Plagioclase is zoned from a andesine core ($Ab_{68}An_{31}Or_{01}$) to an oligoclase rim ($Ab_{83}An_{16}Or_{01}$). White mica contains negligible amounts of Na (0.04–0.07 apfu) and phengite component (Si=3.00–3.10; X_{Mg}>0.5), while biotite is iron-rich with an average X_{Mg} of 0.39 and Ti up to 0.20 apfu. Secondary chlorite has a ripidolite composition with Si=2.72 apfu and an average X_{Mg} (0.40) similar to that of precursor biotite.

Texture and composition of monazite and associated phases

TR2

Monazite appears as relatively large (up to ~300 μm in length) euhedral grains that are mainly included in feldspars and locally occur next to altered mica (Fig. 3a, b). In thin section, monazite occurs in polymineralic textures with a euhedral to subhedral outline (Fig. 3a–c); they contain monazite and minute (<10 μm in diameter) Th–Si-rich phases (hereafter denoted 'ThSi') intergrown with variable amounts of xenotime and apatite. Some textures show slightly spherulitic monazite with only 'ThSi' (Fig. 3a) while others contain a fine-grained mixture of monazite, apatite, xenotime and 'ThSi' (Fig. 3c).

Euhedral monazite grains show BSE-bright, sector- or oscillatory-zoned domains without inclusions that are regarded as primary (Fig. 3d). Those are locally cross-cut by secondary, BSE-darker domains with an irregular outline and numerous inclusions or voids. Some grains preserve a euhedral to subhedral shape with small (<50 μm in size) inclusion-poor domains, but are dominantly BSE-dark and riddled with inclusions and micro-cracks (Fig. 3d). Inclusions in the secondary domains are mainly xenotime and Fe-(hydr)oxide, with minor muscovite and 'ThSi', and rare K-feldspar, quartz, apatite and chloritized biotite. In separated grains, both primary and secondary domains are relatively Y-rich (Y_2O_3=2.53 wt% on average), have comparable UO_2 contents (0.66 vs. 0.55 wt% on average) and contain similar molar fractions of huttonite and cheralite (X_{hut}=3–4 %, X_{cher}=6–8 %). They are best distinguished based on Th and LREE contents (Fig. 4); primary domains have high and variable Th (ThO_2=6.99–19.17 wt%) with Ce_2O_3 averaging at 26.61 wt%, whereas secondary ones contain less Th and Ce (ThO_2=0.80–11.23 wt%, Ce_2O_3=29.12 wt% on average; Table 2).

Quantitative analyses of 'ThSi' phases yield low totals (74–86 wt%, 81.71 wt% on average), which suggests the presence of ~20 wt% H_2O (Table 3). They contain between 36 and 60 wt% ThO_2, 8–14 wt% SiO_2, an average of 7.30 wt% P_2O_5 and 7.05 wt% Y_2O_3, up to 6.38 wt% UO_2, less than 2.5 wt% ($La_2O_3+Ce_2O_3$) and PbO commonly below detection limit (<0.025 wt%). Mineral formulae normalized to four oxygens are compatible with an ATO_4 structure, with Si and P on the 'T' site (Σ=1.02 on average) and Ca, Th, U and REE on the 'A' site (Σ=0.97 on average). Several grains were analyzed by Raman spectroscopy but did not yield any distinct peak, suggesting an amorphous structure.

Large xenotime (up to 150 μm in diameter) was separated together with monazite. It appears as subhedral to rounded grains with relicts of a primary, BSE-bright oscillatory zoning pattern cross-cut by BSE-dark domains that locally contain trails of minute (~1 μm in diameter) uraninite inclusions (Fig. 5a). Primary xenotime domains are generally richer in U, Th and HREE (UO_2=2.12 wt%; ThO_2=0.77 wt%; Σ_{HREE}=0.93 apfu on average) compared to the secondary ones (UO_2=1.17 wt%; ThO_2=0.35 wt%; Σ_{HREE}=0.84 apfu on average; Table 2). Analyses of uraninite inclusions in xenotime are systematically contaminated by the host; they show up to 70 wt% UO_2, 16 wt% ThO_2 and 3 wt% PbO (Table 3).

ZV1

Monazite (100 to 250 μm in length) is commonly found in variably chloritized biotite or at grain boundaries, and locally in quartz or feldspar (Fig. 6a, c). Monazite inside biotite occurs together with apatite, allanite and minor Th–U-rich phases and zircon; the original euhedral outline of the grain is preserved, with an anhedral monazite relict in the core and an apatite aggregate at the rim. This assemblage is surrounded by BSE-bright allanite that grades outward into BSE-darker epidote (Fig. 6a). In the vicinity of chlorite, a network of concentric or cross-cutting allanite and epidote veins is observed (Fig. 6b). Monazite located inside large (<300 μm in diameter) quartz is euhedral and rarely associated with any other phase (Fig. 6c).

Separated monazite is subhedral, exhibits inclusion-poor BSE-bright domains with straight to rounded boundaries (Fig. 6d), and locally contains primary xenotime inclusions. These primary domains are variably replaced by BSE-darker and inclusion-rich secondary domains locally associated with Th–U-rich phases (Fig. 6d). The most common inclusions found in secondary domains are muscovite, apatite and zircon, with minor Fe-(hydr)oxide and rare uraninite or 'ThSi'. Both primary and secondary monazite domains have comparable Y (Y_2O_3=1.56 vs. 1.82 wt% on average) and U (UO_2=1.05 wt%) contents, and a negligible molar fraction of huttonite (X_{hut}=1 % on average). Primary domains are slightly Th-richer than secondary ones (ThO_2=5.64 vs. 4.60 wt%; Fig. 4).

Actinide-rich phases included in the secondary domains are mainly uraninite and locally 'ThSi'. Uraninite contains 62–87 wt% UO_2, 6–23 wt% ThO_2, 3–4.4 wt% PbO, less than 2 wt% Y_2O_3 and has oxide sums between 86 and 99 wt%

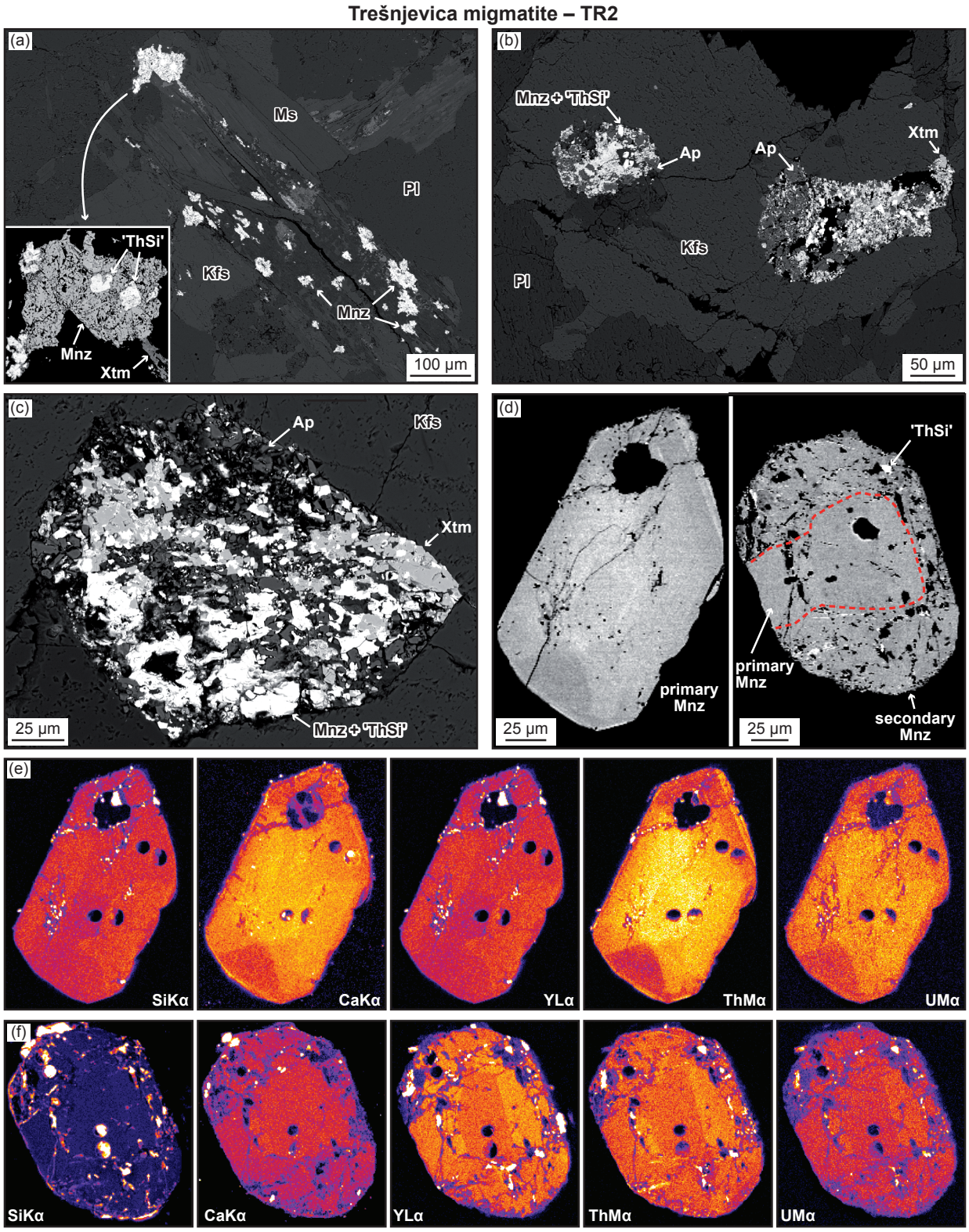

Fig. 3. BSE images of monazite and associated phases in sample TR2. **a** — Monazite with a slight dendritic habitus in and around altered mica, and locally associated with 'ThSi' phases (inset). **b** — Polymineralic assemblages of apatite, xenotime, monazite and 'ThSi' phases (the latter two not distinguishable here) inside K-feldspar. **c** — Detailed view of a polymineralic assemblage (Ap, Xtm, Mnz, 'ThSi') with a euhedral outline inside K-feldspar. **d** — Representative images of primary and secondary monazite domains in separated grains: left, euhedral grain with sector and oscillatory zoning and minor micro-cracks; right, euhedral grain with numerous micro-cracks and inclusions (mainly Xtm) together with scarce 'ThSi' phases. **e, f** — X-ray maps of the monazite grains shown in (d). Warmer colours denote higher intensities; circular holes are pits from laser analyses.

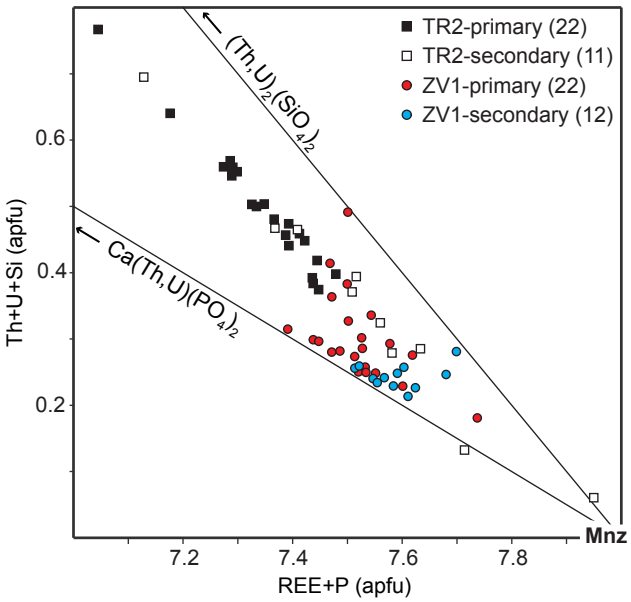

Fig. 4. Composition of primary and secondary monazite domains (samples TR2 and ZV1, number of analyses in brackets) plotted in a Th+U+Si vs. REE+P diagram (cations for 16 oxygens). The "huttonite" and "cheralite" exchange vectors are shown for orientation.

(Table 3). The 'ThSi' phases show (average of two spot analyses) about 50 wt% ThO_2, 10–15 wt% SiO_2, 9 wt% UO_2, 2 wt% Y_2O_3, 0.2 wt% PbO and an oxide sum of 85–90 wt% (Table 3). Valid analyses of epidote-group minerals reveal a composition ranging from REE-rich epidote (Σ_{REE} up to 0.40 apfu) down to epidote with virtually no LREE (Σ_{REE} <0.02 apfu; Table 2). Separated xenotime grains (up to 120 µm in diameter) are euhedral to rounded and preserve inclusion-free, BSE-bright domains with sector or oscillatory zoning. These primary domains are cross-cut by BSE-darker ones with holes and tiny (<2 µm) uraninite or monazite inclusions (Fig. 5b). Primary xenotime domains contain more U and Th (UO_2=2.78 wt%; ThO_2=0.21 wt% on average) than secondary ones (UO_2=1.24 wt%; ThO_2=0.12 wt% on average); they notably show some Pb (PbO=0.04–0.25 wt%) while Pb in the secondary domains is mainly below detection limit (Table 2).

Geochronology

TR2

Microprobe analyses of both primary and secondary monazite domains (33 spots on 22 grains) yield individual Th–U–total Pb dates ranging from 345 to 155 Ma and clustered at ~330 Ma. This main cluster statistically defines a single population with a weighted mean Th–U–total Pb date of 331±3 Ma (n=30, Mean Square Weighted Deviation, MSWD=1.4). One outlier (155 Ma) and two spots with Pb below detection limit were obtained from secondary domains, and the Th–U–total Pb dates of secondary domains tend to be slightly younger than those of primary domains (Fig. 7a). The Th–U–total Pb dates obtained for xenotime are given for orientation; they range from 347 to 271 Ma in primary domains and 380 to 282 Ma (2 spots with Pb below detection limit) in secondary ones. Uraninite inclusions in xenotime yield Th–U–total Pb dates of 338±5, 307±4 and 62±4 Ma (Table 3).

The same monazite spots measured by EPMA were analyzed by LA-ICP-MS (33 spots, 2 rejected). Most analyses are concordant (23 spots) and some indicate initial Pb (Pb_0) contamination (8 spots) at ~350 Ma (Fig. 8a); altogether they define a mixing line between a lower intercept date of 351.1±1.8 Ma and $^{207}Pb/^{206}Pb_0$ of 0.736±0.11 (MSWD=0.95). This result is similar to the weighted average $^{206}Pb/^{238}U$ (350.9±1.9 Ma, MSWD=0.84) and $^{208}Pb/^{232}Th$ (353.6±2.6 Ma, MSWD=0.91) dates calculated with all concordant spots (n=23). Analyses with initial Pb mainly come from secondary monazite domains (6 out of 8; Fig. 8a) and tend to show younger $^{208}Pb/^{232}Th$ dates (337 Ma on average) than the concordant spots. Ten xenotime analyses show no difference between primary and secondary domains, and yield similar weighted average $^{206}Pb/^{238}U$ (352.8±4.6 Ma, MSWD=1.09) and $^{208}Pb/^{232}Th$ dates (349.4±4.3 Ma, MSWD=1.17).

ZV1

Individual Th–U–total Pb dates (34 spots on 16 grains) range from 351 to 253 Ma and cluster at ~325 Ma. The main cluster statistically defines a single population with a weigthed mean Th–U–total Pb date of 329±4 Ma (n=31, MSWD=0.4). The Th–U–total Pb dates of most secondary domains show no difference with those of primary domains, except for three markedly younger spots at ~ 270 Ma (Fig. 7b). The indicative Th–U–total Pb dates of xenotime range from 363 to 281 Ma in primary domains, while only one spot (314 Ma) from secondary domains contains Pb above detection limit. For actinide-rich inclusions in secondary monazite domains, Th–U–total Pb dates range from 360 to 309 Ma (±4 Ma) in uraninite and lie at 73–61±6 Ma in 'ThSi' phases (Table 3).

The same monazite spots measured by EPMA were analyzed by LA-ICP-MS (34 spots, 4 rejected). Most analyses (23 spots) are concordant but show individual $^{206}Pb/^{238}U$ dates scattered from 380 to 339 Ma. Some analyses (7 spots) indicate initial Pb contamination and define, together with the concordant spots, a mixing line between a lower intercept date of 352.8±5.8 Ma and $^{207}Pb/^{206}Pb_0$ of 0.79±0.40 (MSWD=6.8), a rather imprecise result due to the scatter of concordant analyses (Fig. 8b). Concordant analyses yield less scattered individual $^{208}Pb/^{232}Th$ dates that can be used to calculate a statistically better weighted average date of 351.7±2.7 Ma (2 spots rejected, n=21, MSWD=1.19). As for sample TR2, analyses with initial Pb tend to originate from secondary monazite domains (5 out of 7; Fig. 8b). Xenotime analyses show a clear difference between primary domains that are mainly concordant (average $^{206}Pb/^{238}U$ date=354 Ma, 3 spots) and secondary ones with younger and variably discordant results ($^{206}Pb/^{238}U$ dates=338, 215 and 191 Ma, 3 spots).

Table 2: Representative analyses of monazite and xenotime.

Mineral	**Monazite**				**Xenotime**			
Sample	**TR2**		**ZV1**		**TR2**		**ZV1**	
Spot	**001**	**018**	**027**	**034**	**016**	**010**	**006**	**008**
Domain	**primary**	**secondary**	**primary**	**secondary**	**primary**	**secondary**	**primary**	**secondary**
wt % oxides								
SiO_2	1.33	0.71	0.18	0.32	0.64	0.11	0.38	0.24
P_2O_5	28.36	29.43	29.98	29.82	33.06	34.03	33.58	33.91
CaO	0.93	0.89	1.46	1.07	0.04	d.l.	0.20	0.04
ThO_2	9.06	5.41	5.03	4.56	0.63	0.13	0.14	0.10
UO_2	0.69	0.67	2.00	1.08	1.97	0.51	2.53	0.96
Y_2O_3	2.67	2.85	1.94	1.38	39.61	40.41	40.48	41.50
La_2O_3	12.02	12.79	13.68	14.26	n.a.	n.a.	n.a.	n.a.
Ce_2O_3	26.22	28.37	28.48	29.76	n.a.	n.a.	n.a.	n.a.
Pr_2O_3	3.00	3.19	3.15	3.18	n.a.	n.a.	n.a.	n.a.
Nd_2O_3	11.18	11.67	11.73	12.05	0.34	0.44	0.41	0.37
Sm_2O_3	2.22	2.55	1.95	1.83	0.55	0.71	0.59	0.59
Gd_2O_3	2.07	2.20	1.27	1.13	2.10	2.49	1.99	2.02
Tb_2O_3	n.a.	n.a.	n.a.	n.a.	0.63	0.69	0.56	0.54
Dy_2O_3	0.92	1.00	0.51	0.37	5.70	6.03	5.09	5.28
Ho_2O_3	n.a.	n.a.	n.a.	n.a.	3.39	3.63	3.30	3.21
Er_2O_3	n.a.	n.a.	n.a.	n.a.	4.16	4.17	3.98	4.09
Tm_2O_3	n.a.	n.a.	n.a.	n.a.	0.40	0.44	0.45	0.48
Yb_2O_3	n.a.	n.a.	n.a.	n.a.	4.26	3.86	3.69	3.93
Lu_2O_3	n.a.	n.a.	n.a.	n.a.	0.53	0.43	0.41	0.46
PbO	0.17	0.10	0.16	0.11	0.10	d.l.	0.11	d.l.
Total	100.83	101.82	101.51	100.91	98.10	98.08	97.90	97.71
Cations (normalized to 16 oxygens)								
Si	0.210	0.110	0.027	0.049	0.089	0.015	0.053	0.034
P	3.782	3.860	3.933	3.933	3.907	3.983	3.943	3.963
Ca	0.157	0.147	0.243	0.179	0.006	0.000	0.030	0.006
Th	0.325	0.191	0.177	0.162	0.020	0.004	0.004	0.003
U	0.024	0.023	0.069	0.037	0.061	0.016	0.078	0.029
Y	0.223	0.235	0.160	0.114	2.942	2.973	2.987	3.049
La	0.698	0.731	0.782	0.820	–	–	–	–
Ce	1.512	1.609	1.616	1.698	–	–	–	–
Pr	0.172	0.180	0.178	0.180	–	–	–	–
Nd	0.629	0.646	0.649	0.671	0.017	0.021	0.021	0.018
Sm	0.121	0.136	0.104	0.098	0.027	0.034	0.028	0.028
Gd	0.108	0.113	0.065	0.058	0.097	0.114	0.091	0.093
Tb	–	–	–	–	0.029	0.031	0.026	0.025
Dy	0.047	0.050	0.026	0.019	0.256	0.268	0.227	0.235
Ho	–	–	–	–	0.151	0.160	0.146	0.141
Er	–	–	–	–	0.182	0.181	0.173	0.177
Tm	–	–	–	–	0.017	0.019	0.020	0.021
Yb	–	–	–	–	0.181	0.163	0.156	0.165
Lu	–	–	–	–	0.023	0.018	0.017	0.019
Pb	0.007	0.004	0.007	0.004	0.004	0.000	0.004	0.000
Total	8.014	8.036	8.036	8.023	8.008	8.000	8.005	8.005
Mole fractions								
XMnz	0.05	0.02	0.00	0.01				
XCher	0.08	0.07	0.12	0.09				
XHut	0.87	0.91	0.88	0.91				
Th–U–total Pb dates								
Date (Ma)	345	306	329	314	347	–	313	–
±2SD (Ma)	17	23	18	25	82	–	69	–

Notes: n.a.=not analyzed; d.l.=below detection limit

Table 3: Composition of actinide-rich phases found in monazite and xenotime alteration textures.

Spot	Phase	SiO_2	P_2O_5	CaO	FeO	ThO_2	UO_2 (wt%)	Y_2O_3	La_2O_3	Ce_2O_3	PbO	Total	Date (Ma)	±2SD (Ma)
TR2 (average composition of 'ThSi' phases)														
	'ThSi'	11.93	7.30	0.82	n.a.	50.82	2.52	7.05	0.27	1.21	d.l.	81.92	–	–
TR2 (inclusions in secondary xenotime domains)														
001	Urn	0.83	4.31	1.01	d.l.	5.18	70.03	5.31	0.09	1.01	3.00	90.79	307	4
002	Urn	7.42	15.30	2.14	d.l.	2.22	34.90	16.93	d.l.	0.11	d.l.	79.03	–	–
003	'ThSi'+Urn	12.41	4.18	0.15	d.l.	15.96	58.43	3.79	d.l.	0.09	2.42	97.45	281	4
005	Urn	1.37	10.30	0.09	d.l.	12.55	43.98	15.22	d.l.	0.18	2.21	85.92	338	5
006	Urn	7.19	13.18	0.06	d.l.	9.00	31.52	17.03	d.l.	0.07	0.28	78.32	62	4
ZV1 (inclusions in secondary monazite domains)														
001	'ThSi'	14.93	4.07	0.60	d.l.	51.86	9.07	2.56	2.31	5.34	0.21	90.93	61	6
002	'ThSi'	10.18	5.95	0.85	0.08	49.03	9.39	1.75	2.58	5.36	0.24	85.41	73	6
003	Urn	0.63	d.l.	0.12	0.09	18.31	61.64	1.70	0.22	0.54	2.96	86.29	322	4
004	Urn	0.08	d.l.	0.08	d.l.	7.26	81.08	1.74	0.12	0.35	3.52	94.23	309	4
005	Urn	0.21	3.45	0.31	d.l.	9.02	71.68	1.13	1.61	2.81	3.36	93.58	330	4
006	Urn	0.23	d.l.	0.05	d.l.	22.95	64.24	1.59	0.13	0.48	3.33	93.03	341	4
007	Urn	0.06	d.l.	0.05	0.09	5.90	87.21	0.98	0.12	0.36	4.40	99.21	360	4

Notes: n.a. = not analyzed; d.l. = below detection limit. Date = Th–U–total Pb date.

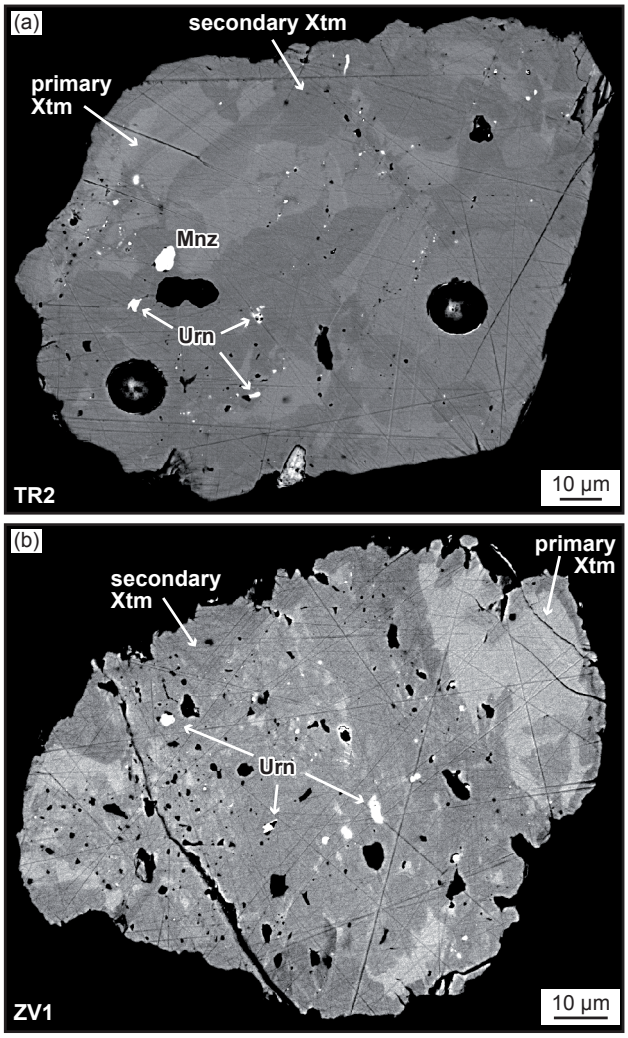

Fig. 5. BSE images of xenotime grains separated from samples TR2 and ZV1, with primary and secondary domains. **a** — TR2: Euhedral xenotime with BSE-bright domains cross-cut by lobate, BSE-darker ones with tiny uraninite inclusions. **b** — ZV1: Subhedral xenotime with relicts of BSE-bright domains replaced by dominant BSE-dark ones containing uraninite inclusions.

Discussion

Monazite and xenotime alteration reactions

The investigated samples were selected because they show different mineralogies, whole-rock compositions and above all contrasting monazite alteration textures. Sample TR2 contains polymineralic pseudomorphs after monazite (Fig. 3), whereas sample ZV1 shows monazite replacement by an apatite–allanite assemblage with a coronitic texture (Fig. 6). In addition, separated monazite and xenotime grains from both samples contain secondary, porous and inclusion-rich domains with little modification of the original grain shape (Figs. 3d, 5 & 6d).

Monazite alteration textures in sample TR2 are characterized by the presence of small (<10 µm) xenotime and Th–Si-rich (±P–Y–U) phases together with secondary monazite (Fig. 3a–c). This assemblage remarkably preserves the original, euhedral shape of primary monazite and might be paralleled with exsolution textures. Following this interpretation, the texture indicates that secondary monazite expelled Th–U and Y during its recrystallization (Fig. 4); these elements were not compatible any more because recrystallization likely occurred at a temperature lower than that of primary monazite formation, which is supported by the tendency for monazite to incorporate more Th (Wiliams et al. 2022) and Y+HREE with increasing temperature (Gratz & Heinrich 1997). This

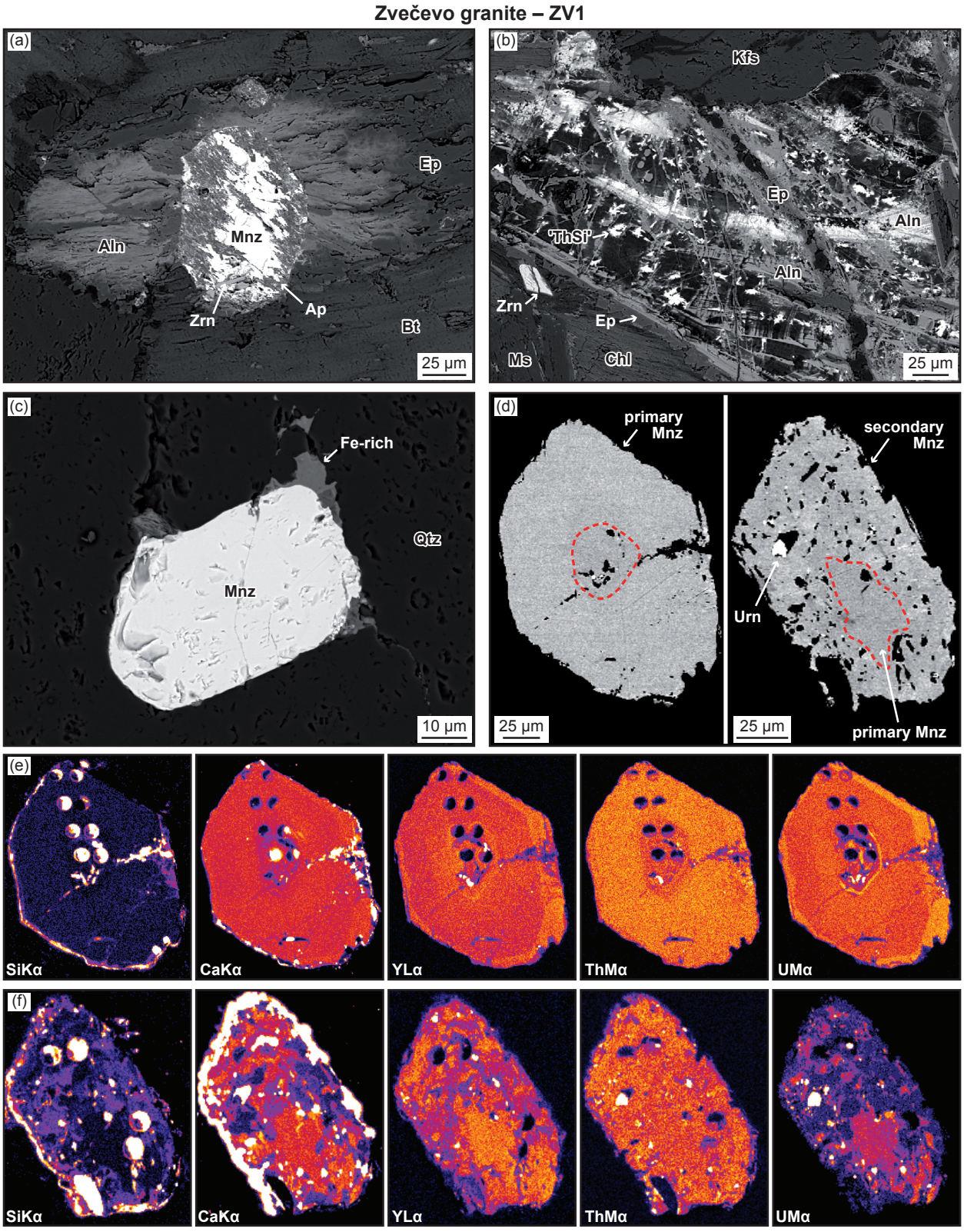

Fig. 6. BSE images of monazite and associated phases in sample ZV1. **a** — Monazite (in slightly chloritized biotite) partially replaced by apatite and surrounded by allanite grading into epidote. **b** — Network of allanite and epidote veinlets between K-feldspar, chlorite and muscovite. **c** — Unaltered, euhedral monazite included in quartz, with tiny Fe-(hydr)oxide at the rim. **d** — Representative images of primary and secondary monazite domains in separated grains: left: euhedral grain with a slightly darker (secondary) core. Right: subhedral grain with numerous inclusions (mainly apatite) and one uraninite. **e, f** — X-ray maps of the monazite grains shown in (d). Warmer colours denote higher intensities; circular holes are pits from laser analyses.

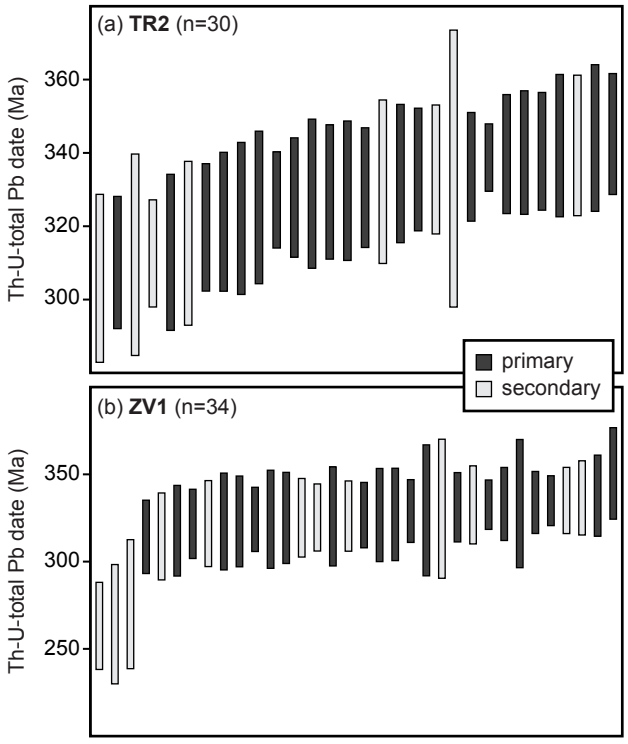

Fig. 7. Results of monazite dating by EPMA for sample TR2 (**a**) (1 outlier at 155 Ma not shown) and ZV1 (**b**). Individual Th–U–total Pb dates are greyscale coded for primary (dark) and secondary (light) monazite domains.

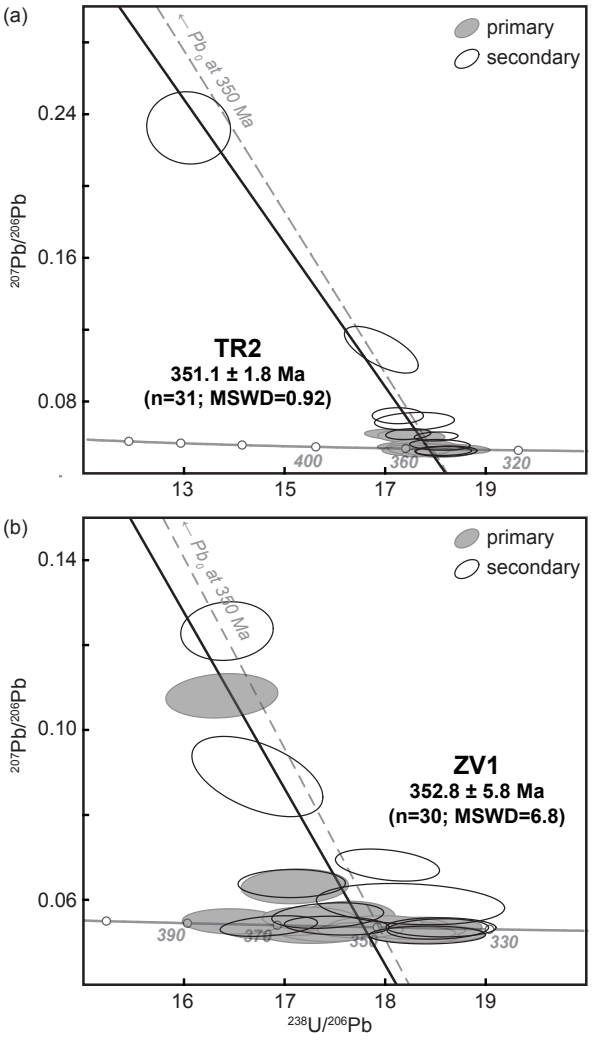

Fig. 8. Results of monazite dating by LA-ICP-MS for sample TR2 (**a**) and ZV1 (**b**) plotted in Tera-Wasserburg diagrams (filled ellipses=primary domains, open ellipses=secondary domains). Lower intercept dates for regressed U–Pb data (full lines) and mixing trends with initial Pb at 350 Ma (0.859 after Stacey & Kramers 1975, dashed lines) are shown.

recrystallization reaction is less commonly found in separated grains, with only a few showing secondary domains with abundant xenotime inclusions. Other in situ textures show variable amounts of apatite around monazite (Fig. 3b, c), which is ascribed to a different reaction (see below).

Monazite alteration in sample ZV1 corresponds to a replacement reaction where apatite and allanite grow at the expense of a former euhedral grain (Fig. 6a). This reaction has already been described, mainly in (meta-)granitoids (e.g., Broska & Siman 1998; Finger et al. 1998; Broska et al. 2005) but also in pegmatite (e.g., Hentschel et al. 2020) or metapelite (e.g., Schulz 2017). Regardless of the lithology, a source of Ca and H_2O (+Si, Al, Fe–Mg) is needed to allow for the reaction (see Gieré & Sorensen 2004). The secondary monazite domains observed in separated grains commonly include apatite (Fig. 6e, f), suggesting that they recrystallized during partial replacement by apatite–allanite. The actinide-rich phases included in secondary monazite likely formed through the same reaction (Fig. 9b).

The dominant alteration texture observed in separated monazite and xenotime from both samples is characterized by BSE-dark secondary domains that irregularly cut across primary zoning patterns (Figs. 3d, 5 & 6d). These secondary domains locally contain trails of holes and actinide-rich phases (Figs. 3f, 5 & 6f). Such features, and especially the curved outline of secondary domains, have been described in products of fluid-bearing alteration experiments (e.g., Williams et al. 2011) as well as in magmatic monazite likely altered in the presence of silicate melt (e.g., Skrzypek et al. 2020). They are commonly ascribed to fluid-mediated recrystallization via a dissolution-reprecipitation process (e.g., Hetherington & Harlov 2008), and the same interpretation is adopted to explain the alteration of most separated grains.

Bulk composition of monazite alteration textures in sample TR2

Because monazite alteration textures observed in TR2 have seldom been described in the literature, their composition was quantified in order to assess element mobility and water content. Mass balance calculations were done with the average compositions (normalized to 100 wt%) of secondary monazite

and xenotime domains (Table 4) and 'ThSi' phases (Table 3; 18.08 wt% H_2O assumed from oxide sum), and the theoretical composition of hydroxylapatite [$Ca_5(PO_4)_3(OH)$]. The volume of individual phases was estimated through image analysis (Fig. 10) with mineral densities of 3.16 g/cm^3 (hydroxylapatite), 4.27 g/cm^3 (xenotime), 5.1 g/cm^3 (monazite) and 7.2 g/cm^3 ('ThSi' phases, assumed to be former huttonite). Black pixels on Fig. 10 correspond to holes derived from removal of material (mainly apatite and monazite, see Figs. 3c & 10c) during polishing or inclusions of the main host phase(s) (mainly quartz and feldspar, Fig. 10b) that were not considered for calculation. The composition (normalized to 100 wt%) of four different textures with increasing apatite content is shown in Table 4 together with the average and range of compositions obtained for primary monazite domains in TR2.

One texture (b1; Fig. 10a) lacks apatite and its re-integrated composition is, for almost all elements except Y, compatible with that of the Th-richest primary domains analyzed in TR2

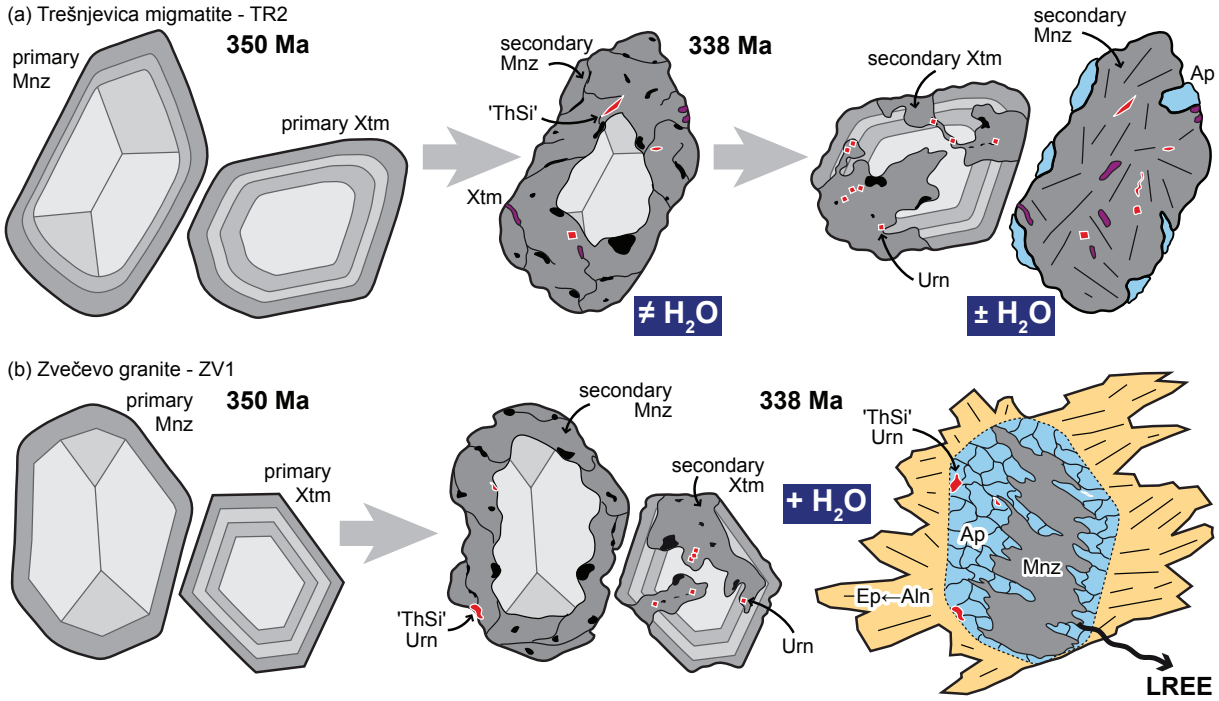

Fig. 9. Schematic sketches summarizing alteration reactions of magmatic monazite and xenotime in Trešnjevica migmatite (**a**) and Zvečevo granite (**b**). Black patches=holes or undifferentiated inclusions.

Table 4: Calculated composition of alteration textures compared to measured compositions in primary monazite domains.

Texture#	b1	a4	a5	a1	Primary monazite domains (wt%)		
Phases & Volume %	Mnz/Xtm/'ThSi' 80/05/15	Ap/Mnz/Xtm/'ThSi' 02/90/02/06	Ap/Mnz/Xtm/'ThSi' 09/87/01/03	Ap/Mnz/Xtm/'ThSi' 21/35/36/08	Average	Min	Max
SiO_2	3.10	1.79	1.35	2.08	1.24	0.68	3.35
P_2O_5	30.79	34.15	35.37	35.78	28.81	25.32	29.88
CaO	0.83	1.67	4.14	8.70	0.99	0.76	1.30
ThO_2	15.14	9.94	8.12	9.25	8.87	6.67	19.17
UO_2	1.08	0.83	0.72	1.09	0.66	0.44	1.00
Y_2O_3	5.85	4.02	2.90	20.20	2.70	2.25	3.25
La_2O_3	12.26	14.31	14.43	6.27	12.16	10.40	13.22
Ce_2O_3	27.27	31.73	31.99	13.96	26.61	21.17	28.56
PbO	0.11	0.12	0.12	0.09	0.15	0.11	0.32
H_2O	3.56	1.44	0.86	2.58	–	–	–
H_2O*	0	0.03	0.11	0.27	–	–	–

All alteration textures in wt% normalized to 100. H_2O*=water content assuming that ['ThSi' phases were originally anhydrous.
Input compositions=average of secondary domain analyses (wt% normalized to 100):

Mnz. SiO_2=0.95, P_2O_5=36.18, CaO=0.88, ThO_2=6.71, UO_2=0.68, Y_2O_3=2.69, La_2O_3=16.11, Ce_2O_3=35.67, PbO=0.13

Xtm. SiO_2=0.55, P_2O_5=43.22, CaO=0, ThO_2=0.44, UO_2=1.50, Y_2O_3=54.19, $La2O_3$=0, Ce_2O_3=0, PbO=0.10

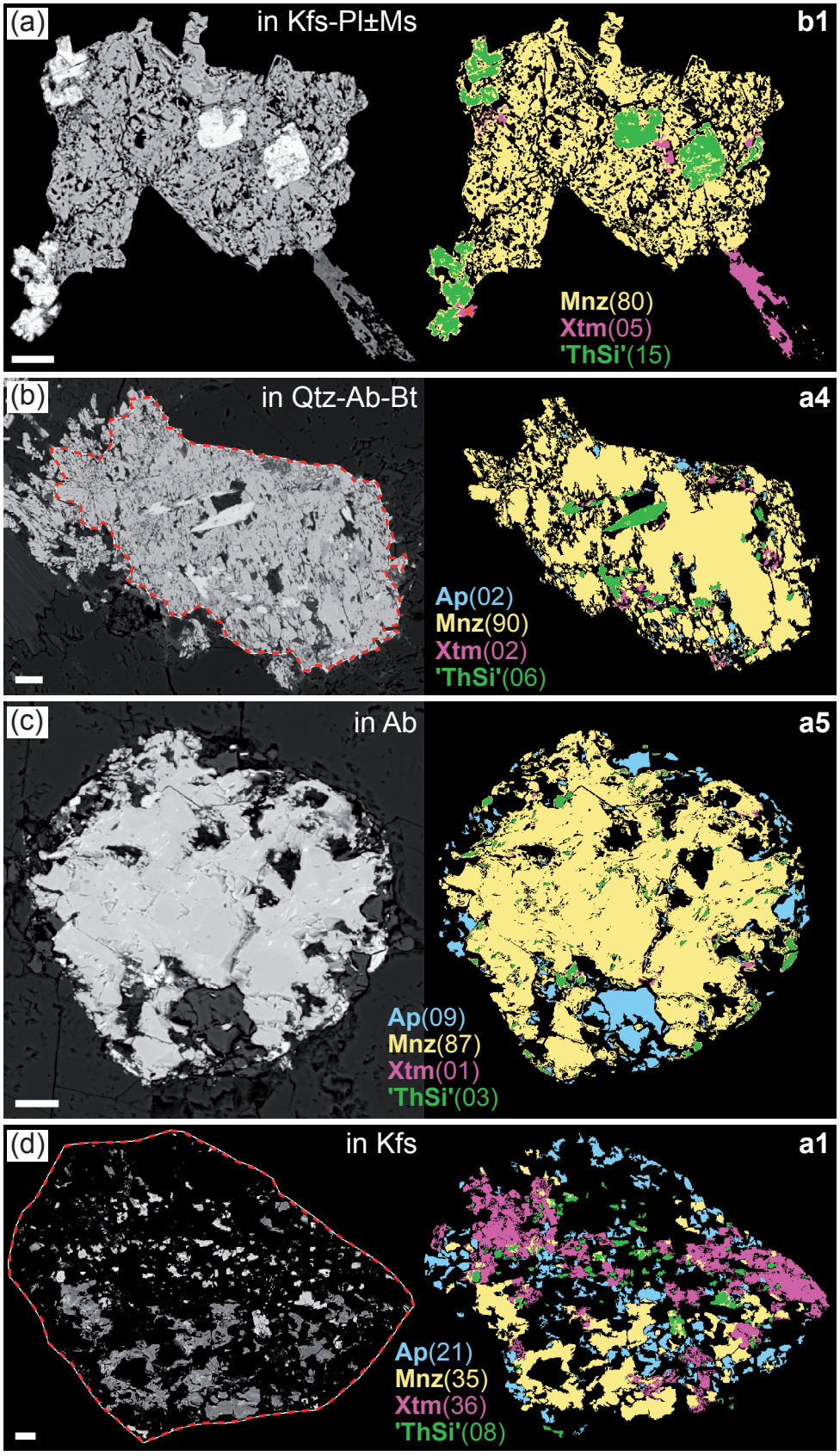

Fig. 10. BSE images (left) of monazite alteration textures in sample TR2 and composite images (right) illustrating the volume proportions (in %) estimated by image analysis. Texture names refer to those in Table 4. The red dashed line in (**b**, **d**) outlines the area used for image analysis. Scale bar is always 10 μm.

(Table 4). The relatively high Y content could be explained by Y mobility, which is supported by elongate xenotime growing outside the main texture (Fig. 10a). Two other textures (a4 & a5; Fig. 10b, c) contain little apatite (2–9 vol%) and are, apart from P and Ca, similar in composition to the average of primary domains (Table 4). Again, high Y values may indicate Y mobility or derive from xenotime initially present with primary monazite. Another texture (a1; Fig. 10d) contains significantly more apatite (21 vol%) and its bulk composition departs from that of primary monazite, especially for Ca, Y, and LREE (Table 4). The high proportion of xenotime (36 vol%) suggests that it might have been originally present before alteration.

Element mobility during alteration

For most textures in sample TR2, the re-integrated composition is compatible with that of a Th–Y-rich monazite precursor that decomposed to xenotime, 'ThSi' phases and Th–Y-poorer secondary monazite (Fig. 9a). This demonstrates the isochemical character of the reaction and the efficient trapping of LREE and actinides at the location of the original monazite grain. Only the results for Y suggest some mobility, in agreement with the pervasive alteration of primary xenotime (Fig. 5a). In the case of low-concentration elements like U and Pb, the results of mass balance calculations will strongly depend on assumed compositions for monazite and 'ThSi' phases. We can nevertheless note that re-integrated UO_2 concentrations lie in the range of those of primary monazite (Table 4), whereas PbO is systematically lower and suggests Pb loss during alteration or subsequent metamictization. Some textures in TR2 contain a relatively high proportion of apatite (up to 21 vol%) and point to Ca, P and H_2O input. Because such textures are found inside Ca-free minerals (Kfs, Ab, Qtz, Bt), they likely indicate the mediation of a fluid phase (Fig. 9a).

The chemical budget of monazite replacement by apatite–allanite has already been discussed by Finger et al. (1998). They remarked that, for major elements in monazite (excluding Si and Ca), the replacement reaction is mainly isochemical, although the associated texture clearly contains two distinct zones. The inner zone has exactly the shape of the primary monazite grain and indicates a relative immobility of P and Th–U stored in apatite and actinide-rich phases, respectively (Fig. 6a). The outer zone consists of epidote with variable REE content and clearly points to outward REE migration, in some cases even farther from the original monazite (Fig. 6b), which hints at the presence of a fluid phase (Fig. 9b).

Role of fluid and whole-rock composition

The re-integrated compositions of alteration textures in TR2 yield H_2O contents between 0.86 and 3.56 wt% (Table 4). These values mainly derive from the relatively high H_2O content (~18 wt%) assumed to be present in 'ThSi' phases based on their low oxide sum. However, several workers describe alteration textures of actinide-bearing minerals that contain anyhdrous Th±U-rich phases (e.g., Harlov et al. 2007; Berger et al. 2009; Budzyń et al. 2020), so that one could consider the hydration of 'ThSi' phases as a later process (e.g., Stachowicz et al. 2024), probably facilitated by metamictization (e.g., Lumpkin & Chakoumakos 1988). If 'ThSi' phases are assumed to be originally anhydrous, the amount of H_2O in the quantified textures drops to less than 0.3 wt% and is theoretically null in apatite-free ones (Table 4). This is used to propose a negligible role of fluids in the observed decomposition of monazite, especially because the spatial distribution of secondary products does not seem to indicate the presence of a former fluid pathway (Fig. 10). Conversely, the formation of apatite at the rim of the decomposition texture does indicate (later?) addition of H_2O together with Ca and P. We can further speculate that micro-cracks and alteration haloes that are typical around actinide-bearing inclusions facilitated fluid flow and element supply (e.g., Procházka et al. 2011). The alteration textures observed in most separated grains, inferred to result from dissolution–reprecipitation, represent another argument for the presence of a fluid phase.

In sample ZV1 the replacement of monazite by apatite–allanite, i.e. two hydrous minerals, obviously requires H_2O input. To explain this texture Broska & Siman (1998) invoke the mediation of a fluid associated with the breakdown of biotite and Ca-bearing plagioclase, perhaps during post-magmatic hydrothermal alteration (e.g., Ondrejka et al. 2012). This is in agreement with the observation of apatite–allanite around monazite included in variably chloritized biotite (Fig. 6a), whereas monazite armoured inside quartz remained intact (Fig. 6c). We can mention for comparison that a texture with 25 % allanite, 25 % hydroxylapatite and 50 % monazite (volume proportions) would theoretically contain about 1.3 wt% H_2O while a complete replacement by ~50:50 % allanite–hydroxylapatite would host 3.2 wt% H_2O, i.e. nearly the amount that is contained in biotite.

The difference in monazite alteration reactions chiefly reflects the contrast in sample mineralogy and initial monazite composition. On the one hand, a "dry" monazite decomposition is interpreted to have taken place in the migmatite sample (TR2) because Th-rich (ThO_2=6.99–19.17 wt%) primary grains are commonly included in mm-sized, anhydrous major minerals (Fig. 3b, c) and could hardly be reached by fluids. The paucity of hydrous minerals and the low Ca whole-rock content (Table 1) additionally explain the limited, post-magmatic production of in situ fluids and the relative stability of monazite (e.g., Janots et al. 2008). On the other hand, a "wet" replacement of Th-poorer (ThO_2=3.29–7.20 wt%) monazite by hydrous minerals occurred in the granite sample (ZV1), which itself contains all ingredients for the inferred reaction. It is relatively rich in Ca (CaO=1.49 wt%), which favours allanite stability in granitoids (e.g., Broska et al. 2024), and the alteration of Ca-rich plagioclase cores (andesine) could have mobilized Ca while micas liberated H_2O. Assuming that the reaction was associated with biotite chloritization requires

more H_2O than what is available in magmatic micas, but the observed monazite textures do not represent a particular sink for such an additional fluid.

Aqueous fluid is clearly a *reactant* when anhydrous monazite and xenotime are partly replaced by hydrous phases like apatite or allanite (e.g., Broska & Siman 1998). Conversely, it never appears to be a reaction *product*; recrystallization textures ascribed to fluid-mediated dissolution–precipitation lack free H_2O (e.g., Hetherington & Harlov 2008; Budzyń et al. 2023), unless the abundant pores are regarded as former fluid inclusions. This suggests that fluid is mainly a *catalyst* (Putnis & Putnis 2007), whose former presence is perhaps best inferred from the irregular shape of altered domains or the chemical budget of reactions. For example, apatite–epidote coronas are not truly isochemical at the scale of the original monazite grain; they need a fluid phase for (limited) element (mainly REE) transport outward. In contrast, the nearly isochemical polymineralic pseudomorphs observed in sample TR2 lack evidence for fluid mediation.

Timing of alteration

Primary monazite in both samples has several features indicating growth from a melt. It is euhedral, shows sector- or oscillatory zoning and contains few, if any, inclusions (Figs. 3 & 6), which is common in magmatic monazite (e.g., Skrzypek et al. 2020; Schulz 2021). Dating of primary domains yields a single population of Th–U–total Pb and U–Th/Pb dates indicating a single growth event. Th–U–total Pb dates tend to be slightly younger than U–Th/Pb ones (Figs. 7 & 8), which might be attributed to the relatively high detection limit of the EPMA for Pb (~150 ppm), especially for samples younger than ~500 Ma, but also to the presence of initial Pb (Fig. 8) that can slightly affect $^{206}Pb/^{238}U$ dates. Facing a similar issue, Santitharangkun et al. (2025) recommended regarding the oldest Th–U–total Pb dates as the most accurate, which in the present case fairly reconciles both EPMA and LA-ICP-MS results. For sample TR2, the weighted average $^{206}Pb/^{238}U$ date of 350.9±1.9 Ma (final uncertainty=9.0 Ma) is regarded as the age of melt crystallization in migmatite. For sample ZV1, the weighted average $^{208}Pb/^{232}Th$ date of 351.7±2.7 Ma (final uncertainty=9.2 Ma) is interpreted to best approximate the age of granite crystallization (Fig. 11), whereas individual $^{206}Pb/^{238}U$ dates show a broader scatter (380–339 Ma). The latter might reflect some inherited Pb component, which is supported by the common occurrence of xenocrystic cores in magmatic zircon from the same sample. Both ages are similar and point to coeval partial melting and granitoid intrusion in the middle crust during Variscan orogeny (Pamić & Lanphere 1991).

The formation of secondary monazite and xenotime domains through recrystallization can be used to assess the timing of alteration. In TR2 the average $^{208}Pb/^{232}Th$ date of secondary monazite domains (340 Ma) agrees with the oldest Th–U–total Pb date (338±5 Ma) of uraninite inclusions in secondary xenotime (Fig. 11). In ZV1 the oldest concordant spot from secondary xenotime domains ($^{206}Pb/^{238}U$ date=338±12 Ma) matches the average Th–U–total Pb date (332 Ma) of uraninite inclusions in secondary monazite (Fig. 11). This accumulation of similar dates suggests monazite and xenotime alteration at ca. 335 Ma during a late phase of Variscan orogeny. A thermal event, probably at subsolidus temperature conditions, triggered monazite recrystallization in both samples, as also suggested by K–Ar ages reported for Papuk complex (Pamić et al. 1988). Interestingly, a similar monazite record of magmatic activity at ~350 Ma followed by an early Carboniferous thermal event (~330 Ma) is reported in the Western Carpathians (e.g., Broska et al. 2022), on the northern side of the extension-related Pannonian basin (Fig. 1).

An Alpine overprint is documented in crystalline rocks of the Slavonian Mountains (e.g., Balen et al. 2013, 2018a) and could also be responsible for a partial resetting of Carboniferous monazite and xenotime (Fig. 11). However, this would be expected to generate at least a few Cretaceous dates, especially if new domains recrystallized at that time, but none were detected in secondary monazite or xenotime. Only actinide-rich phases might indicate an Alpine event, with Th–U–total Pb results of 62±4 Ma in one uraninite (in Xtm) from TR2 and 73–61±6 Ma in two 'ThSi' phases (in Mnz) from ZV1 (Fig. 11). Berger et al. (2008) discussed the geochronological potential of actinide-rich phases in alteration textures and recognized that they might incorporate initial Pb or easily loose radiogenic Pb. The latter process likely explains the negligible amount of Pb in 'ThSi' phases from sample TR2. It is finally noteworthy that, although both uranium- and thorium-rich phases occur in alteration textures, only uraninite confidently preserves the timing of alteration (Fig. 11), suggesting a better resistance of U-oxide than Th-silicate to Pb loss and, presumably, to radiation damage.

Conclusions

Two contrasting alteration textures are identified in crystalline rocks from Mt. Papuk (Croatia). The first one is interpreted to be the result of a "dry" decomposition of primary magmatic monazite into secondary monazite, Th–Si-rich phases and xenotime. It is observed in a Ca-poor, nebulitic migmatite with few hydrous minerals, and lacks evidence for the mediation of a fluid phase. It is locally rimmed by apatite ascribed to subsequent, but limited, fluid input. The second one derives from a "wet" monazite replacement by apatite and allanite together with the formation of some recrystallized secondary monazite domains. It is found in a Ca-richer, two-mica granite sample and fully matches corona textures previously described in granitoids affected by post-magmatic overprints. The formation of secondary monazite and xenotime domains through dissolution-reprecipitation is also recognized.

Dating of primary monazite domains yields, for both samples, a similar age of ca. 350 Ma ascribed to monazite crystallization from melt in migmatite and granite, respectively.

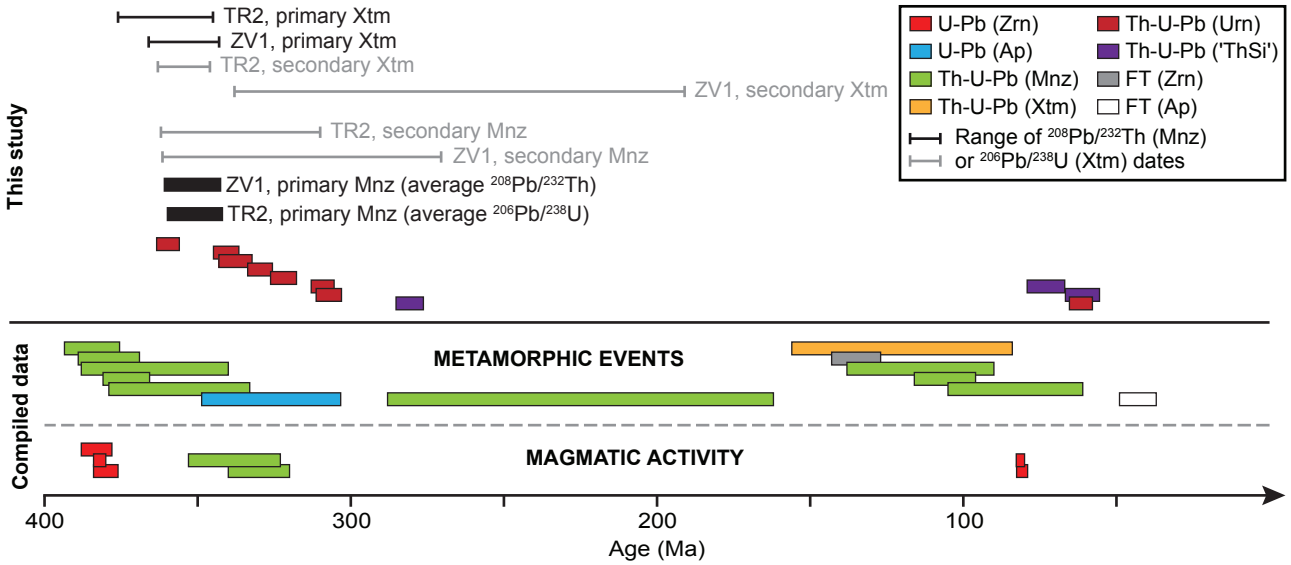

Fig. 11. Overview of igneous and metamorphic events in the Slavonian Mts. based on geochronological results selected for the period 400–0 Ma. Compiled data are after Horváth et al. (2010), Ustaszewksi et al. (2010), Biševac et al. (2011, 2013), Balen et al. (2013, 2018a, b), Horvat et al. (2018), Balen & Massone (2020), Schneider et al. (2022, 2025), and are available in Supplementary Table S3.

The secondary monazite and xenotime domains are slightly younger (ca. 335 Ma), contain tiny uraninite inclusions with similar dates, and suggest late Variscan alteration during a medium-temperature thermal event rather than resetting during an Alpine overprint.

The general implication is that primary Th–Y-rich monazite will break down when subject to *P–T* conditions differing from those of its formation, regardless of fluid availability. If little or no fluid is present, it will expel actinides and Y+HREE in its immediate vicinity. If fluid is present, its replacement will efficiently retain P and actinides but might lead to LREE mobility, at least on the millimetre scale. The amount of H_2O present in both alteration textures does not exceed 4 wt%, indicating that these do not act as major sinks for fluids. In order to date the alteration of actinide-bearing minerals like monazite, tiny U-oxides are more reliable than Th-silicates.

Acknowledgments: The contribution stems from the project "Old orogeny and young magmatism: Cretaceous dyke swarms and their relations to the Variscan basement (Mt. Papuk, Croatia)" that was financially supported by the ÖAD through a WTZ Austria-Croatia grant to D. Gallhofer (HR 16/2024) and MZOM Scientific & Technological cooperation to D. Balen. B. Budzyń is thanked for kindly providing fragments of TS-Mnz monazite. K. Bischof, A. Pock and S. Meschnark are thanked for sample preparation. We acknowledge constructive comments by Igor Petrík, Michael Williams and an anonymous reviewer, and editorial handling by Milan Kohút. We finally congratulate Igor Broska for his career and thank him for his numerous and inspiring works on the petrogenesis of accessory minerals.

References

Aleinikoff J.N., Schenck W.S., Plank M.O., Srogi L., Fanning C.M., Kamo S.L. & Bosbyshell H. 2006: Deciphering igneous and metamorphic events in high-grade rocks of the Wilmington Complex, Delaware: Morphology, cathodoluminescence and backscattered electron zoning, and SHRIMP U–Pb geochronology of zircon and monazite. *GSA Bulletin* 118, 39–64. https://doi.org/10.1130/B25659.1

Balen D. & Massonne H.-J. 2020: Variscan monazite ages and peak metamorphic P-T conditions recorded in gneiss/migmatite from the Pannonian Basin Basement (Mt. Papuk, Croatia). In: 22nd EGU General Assembly, held online 4-8 May, 2020, id.2621. https://doi.org/10.5194/egusphere-egu2020-2621

Balen D., Horváth P., Tomljenović B., Finger F., Humer B., Pamic J. & Árkai P. 2006: A record of pre-Variscan Barrovian regional metamorphism in the eastern part of the Slavonian Mountains (NE Croatia). *Mineralogy and Petrology* 87, 143–162. https://doi.org/10.1007/s00710-006-0120-1

Balen D., Horváth P., Finger F. & Starijaš B. 2013: Phase equilibrium, geothermobarometric and xenotime age dating constraints on the Alpine metamorphism recorded in chloritoid schists from the southern part of the Tisia Mega-Unit (Slavonian Mts., NE Croatia). *International Journal of Earth Sciences* 102, 1091–1109. https://doi.org/10.1007/s00531-012-0850-8

Balen D., Massonne H.-J. & Petrinec Z. 2015: Collision-related Early Paleozoic evolution of a crustal fragment from the northern Gondwana margin (Slavonian Mountains, Tisia Mega-Unit, Croatia): Reconstruction of the P–T path, timing and paleotectonic implications. *Lithos* 232, 211–228. https://doi.org/10.1016/j.lithos.2015.07.003

Balen D., Massonne H.-J. & Lihter I. 2018a: Alpine metamorphism of low-grade schists from the Slavonian Mountains (Croatia): new P–T and geochronological constraints. *International Geology Review* 60, 288–304. https://doi.org/10.1080/00206814.2017.1328710

Balen D., Schneider P., Opitz J. & Massonne H.J. 2018b: Ages and Trace Element Patterns of Apatite and Zircon in a Diorite from the Mt. Papuk metamorphic complex (Pannonian Basin Basement in Croatia, CE Europe). In: *AGU Fall Meeting Abstracts*, V33E-0285.

Be Mezeme E.B., Cocherie A., Faure M., Legendre O. & Rossi P. 2006: Electron microprobe monazite geochronology of magmatic events: examples from Variscan migmatites and granitoids, Massif Central, France. *Lithos* 87, 276–288.

Bence A.E. & Albee A.L. 1968: Empirical correction factors for the electron microanalysis of silicates and oxides. *Journal of Geology* 76, 382–403.

Berger A., Gnos E., Janots E., Fernandez A. & Giese J. 2008: Formation and composition of rhabdophane, bastnäsite and hydrated thorium minerals during alteration: Implications for geochronology and low-temperature processes. *Chemical Geology* 254, 238–248. https://doi.org/10.1016/j.chemgeo.2008.03.006

Berger A., Rosenberg C. & Schaltegger U. 2009: Stability and isotopic dating of monazite and allanite in partially molten rocks: Examples from the Central Alps. *Swiss Journal of Geosciences* 102, 15–29. https://doi.org/10.1007/s00015-009-1310-8

Biševac V., Krenn E., Balen D., Finger F. & Balogh K. 2011: Petrographic, geochemical and geochronological investigation on granitic pebbles from Permotriassic metasediments of the Tisia terrain (eastern Papuk, Croatia). *Mineralogy and Petrology* 102, 163–180. https://doi.org/10.1007/s00710-011-0175-5

Biševac V., Krenn E., Finger F., Lužar-Oberiter B. & Balen D. 2013: Provenance of Paleozoic very low-to low-grade metasedimentary rocks of South Tisia (Slavonian Mountains, Radlovac Complex, Croatia). *Geologica Carpathica* 64, 3–22. https://doi.org/10.2478/geoca-2013-0001

Bosse V., Boulvais P., Gautier P., Tiepolo M., Ruffet G., Devidal J.L., Cherneva Z., Gerdjikov I. & Paquette J.L. 2009: Fluid-induced disturbance of the monazite Th–Pb chronometer: In situ dating and element mapping in pegmatites from the Rhodope (Greece, Bulgaria). *Chemical Geology* 261, 286–302. https://doi.org/10.1016/j.chemgeo.2008.10.025

Broska I. & Siman P. 1998: The breakdown of monazite in the West-Carpathian Veporic orthogneisses and Tatric granites. *Geologica Carpathica* 49, 161–167.

Broska I., Williams C.T., Janák M. & Nagy G. 2005: Alteration and breakdown of xenotime-(Y) and monazite-(Ce) in granitic rocks of the Western Carpathians, Slovakia. *Lithos* 82, 71–83. https://doi.org/10.1016/j.lithos.2004.12.007

Broska I., Janák M., Svojtka M., Yi K., Konečný P., Kubiš M., Kurylo S., Hrdlička M. & Maraszewska M. 2022: Variscan granitic magmatism in the Western Carpathians with linkage to slab break-off. *Lithos* 412–413, 106589. https://doi.org/10.1016/j.lithos.2021.106589

Broska I., Petrík I., Yi K., Majka J., Barnes C.J., Vojtko R., Madarás J., Kurylo S. & Kubiš M. 2024: Alpine stacking of two Variscan granite blocks recognised from mineral stabilities, age and structural data (Western Carpathians). *Chemical Geology* 648, 121959. https://doi.org/10.1016/j.chemgeo.2024.121959

Budzyń B., Birski Ł., Wirth R. & Schreiber A. 2020: Nanoscale constraints on a fluid-induced transformation of monazite during postmagmatic alteration–A case of the Jawornik granitoid (NE Orlica-Śnieżnik Dome, Sudetes, SW Poland). *Lithos* 376, 105777. https://doi.org/10.1016/j.lithos.2020.105777

Budzyń B., Sláma J., Corfu F., Crowley J., Schmitz M., Williams M. L., Jercinovic M.J., Kozub-Budzyń G.A., Konečny P., Rzepa G. & Włodek A. 2021: TS-Mnz – A new monazite age reference material for U–Th–Pb microanalysis. *Chemical Geology* 572, 120195. https://doi.org/10.1016/j.chemgeo.2021.120195

Budzyń B., Wirth R., Sláma J., Kozub-Budzyń G.A., Konečný P., Rzepa G. & Schreiber A. 2023: Micro- to nanoscale constraints on metasomatic alterations of xenotime, inclusions of Th-, U- and Pb-phases and their geochronological implications (Ås pegmatite, Evje and Hornnes, S Norway). *Chemical Geology* 632, 121538. https://doi.org/10.1016/j.chemgeo.2023.121538

Catlos E.J. 2013: Generalizations about monazite: Implications for geochronologic studies. *American Mineralogist* 98, 819–832. https://doi.org/10.2138/am.2013.4336

Didier A., Bosse V., Boulvais P., Bouloton J., Paquette J. L., Montel J. M. & Devidal J. L. 2013: Disturbance versus preservation of U–Th–Pb ages in monazite during fluid-rock interaction: Textural, chemical and isotopic in situ study in microgranites (Velay Dome, France). *Contributions to Mineralogy and Petrology* 165, 1051–1072. https://doi.org/10.1007/s00410-012-0847-0

Dini A., Rocchi S. & Westerman D.S. 2004: Reaction microtextures of REE–Y–Th–U accessory minerals in the Monte Capanne pluton (Elba Island, Italy): a possible indicator of hybridization processes. *Lithos* 78, 101–118. https://doi.org/10.1016/j.lithos.2004.04.045

Engi M. 2017: Petrochronology based on REE-minerals: monazite, allanite, xenotime, apatite. *Reviews in Mineralogy and Geochemistry* 83, 365–418. https://doi.org/10.2138/rmg.2017.83.12

Evans J.A., Zalasiewicz J.A., Fletcher I., Rasmussen B. & Pearce N. J.G. 2002: Dating diagenetic monazite in mudrocks: constraining the oil window? *Journal of the Geological Society, London* 159, 619–622.

Finger F., Broska I., Roberts M.P. & Schermaier A. 1998: Replacement of primary monazite by apatite-allanite-epidote coronas in an amphibolite facies granite gneiss from the eastern Alps. *American Mineralogist* 83, 248–258.

Förster H.-J. 2001: Synchysite-(Y)–synchysite-(Ce) solid solutions from Markersbach, Erzgebirge, Germany: REE and Th mobility during high-T alteration of highly fractionated aluminous A-type granites. *Mineralogy and Petrology* 72, 259–280.

Franke W. 2000: The mid-European segment of the Variscides: tectonostratigraphic units, terrane boundaries and kinematic evolution. In: Franke W., Haak V., Oncken O. & Tanner D. (Eds.): Orogenic Processes: Quantification and Modelling in the Variscan Belt. *Geological Society Special Publication* 179, 35–63. https://doi.org/10.1144/GSL.SP.2000.179.01.05

Friedl G., von Quadt A., Ochsner A. & Finger F. 1993: Timing of the Variscan orogeny in the Southern Bohemian Massif (NE Austria) deduced from new U–Pb zircon and monazite dating. *Terra Nova* 5, 235–236.

Friedl G., von Quadt A. & Finger F. 1996: Timing der Intrusionstätigkeit im Südböhmischen Batholith. In: Abstract 6. Symposium Tektonik–Strukturgeologie–Kristallingeologie, 127–130.

Gieré R. & Sorensen S.S. 2004: Allanite and other: REE-rich epidote-group minerals. *Reviews in Mineralogy and Geochemistry* 56, 431–493. https://doi.org/10.2138/gsrmg.56.1.431

Goncalves P., Nicollet C. & Montel J.-M. 2004: Petrology and in situ U–Th–Pb Monazite Geochronology of Ultrahigh-Temperature Metamorphism from the Andriamena Mafic Unit, North–Central Madagascar. Significance of a Petrographical P–T Path in a Polymetamorphic Context. *Journal of Petrology* 45, 1923–1957. https://doi.org/10.1093/petrology/egh041

Gonçalves G.O., Lana C., Scholz R., Buick I.S., Gerdes A., Kamo S.L., Corfu F., Marinho M.M., Chaves A.O., Valeriano C. & Nalini H.A. 2016: An assessment of monazite from the Itambé pegmatite district for use as U–Pb isotope reference material for microanalysis and implications for the origin of the "Moacyr" monazite. *Chemical Geology* 424, 30–50. https://doi.org/10.1016/j.chemgeo.2015.12.019

Gratz R. & Heinrich W. 1997: Monazite–xenotime thermobarometry: Experimental calibration of the miscibility gap in the binary system $CePO_4$–YPO_4. *American Mineralogist* 82, 772–780.

Harlov D.E. & Hetherington C.J. 2010: Partial high-grade alteration of monazite using alkali-bearing fluids: Experiment and nature. *American Mineralogist* 95, 1105–1108. https://doi.org/10.2138/am.2010.3525

Harlov D.E., Marschall H.R. & Hanel M. 2007: Fluorapatite–monazite relationships in granulite-facies metapelites, Schwarzwald, southwest Germany. *Mineralogical Magazine* 71, 223–234. https://doi.org/10.1180/minmag.2007.071.2.223

Harlov D.E., Wirth R. & Hetherington C.J. 2011: Fluid-mediated partial alteration in monazite: The role of coupled dissolution-reprecipitation in element redistribution and mass transfer. *Contributions to Mineralogy and Petrology* 162, 329–348. https://doi.org/10.1007/s00410-010-0599-7

Harlov D.E., Meighan C.J., Kerr I.D. & Samson I.M. 2016: Minera logy, Chemistry, and Fluid-Aided Evolution of the Pea Ridge Fe Oxide-(Y + REE) Deposit, Southeast Missouri, USA. *Economic Geology* 111, 1963–1984. https://doi.org/10.2113/econgeo.111.8.1963

Harlov D., Ballouard C., Elburg M., Knoper M., Wilke F., Ning W.B. & Andreoli M.A.G. 2020: Genesis of monazite-rich, orthopyroxene-bearing veins in the Kliphoog area of the Concordia Granite, Springbok, Namaqualand, South Africa: Sources, fluids, and the mobility of actinides and REE. *Lithos* 376–377, 105762. https://doi.org/10.1016/j.lithos.2020.105762

Harrison T.M., Catlos E.J. & Montel J.-M. 2002: U–Th–Pb dating of phosphate minerals. *Reviews in Mineralogy and Geochemistry*. 48, 524–558. https://doi.org/10.2138/rmg.2002.48.14

Heinrich W., Rehs G. & Franz G. 1997: Monazite–xenotime miscibility gap thermometry. I. An empirical calibration. *Journal of Metamorphic Geology* 15, 3–16.

Hentschel F., Janots E., Trepmann C.A., Magnin V. & Lanari P. 2020: Corona formation around monazite and xenotime during greenschist-facies metamorphism and deformation. *European Journal of Mineralogy* 32, 521–544. https://doi.org/10.5194/ejm-32-521-2020

Hetherington C.J. & Harlov D.E. 2008: Metasomatic thorite and uraninite inclusions in xenotime and monazite from granitic pegmatites, Hidra anorthosite massif, southwestern Norway: Mechanics and fluid chemistry. *American Mineralogist* 93, 806–820. https://doi.org/10.2138/am.2008.2635

Horvat M., Klötzli U., Jamičić D., Buda G., Klötzli E. & Hauzenberger C. 2018: Geochronology of granitoids from Psunj and Papuk Mts., Croatia. *Geochronometria* 45, 198–210. https://doi.org/10.1515/geochr-2015-0099

Horváth P., Balen D., Finger F., Tomljenović B. & Krenn E. 2010: Contrasting *P–T–t* paths from the basement of the Tisia Unit (Slavonian Mts., NE Croatia): Application of quantitative phase diagrams and monazite age dating. *Lithos* 117, 269–282. https://doi.org/10.1016/j.lithos.2010.03.004

Jamičić D. 1983: Strukturni sklop metamorfnih stijena Krndije i južnih padina Papuka [Structural fabric of the metamorphosed rocks of Mt. Krndija and the eastern part of Mt. Papuk]. *Geološki vjesnik* 36, 51–72 (in Croatian).

Jamičić D. 1988: Strukturni sklop slavonskih planina [Tectonics of the Slavonian Mts.]. *PhD thesis, University of Zagreb*, Zagreb, 1–152 (in Croatian).

Jamičić D. 1989: Basic geological map of Yugoslavia in scale 1:100,000, sheet Daruvar. *Geological Institute Zagreb, Federal Geological Institute*, Belgrade.

Jamičić D. & Brkić M. 1987: Basic geological map of Yugoslavia in scale 1:100,000, sheet Orahovica: *Geological Institute Zagreb, Federal Geological Institute*, Belgrade.

Jamičić D., Brkić M., Crnko, J. & Vragović M. 1987: Basic geological map of Yugoslavia – Explanatory notes for sheet Orahovica: *Geological Institute Zagreb, Federal Geological Institute*, Belgrade.

Jamičić D., Vragović M. & Matičec D. 1989: Basic Geological Map of Yugoslavia – Explanatory notes for sheet Daruvar: *Geological Institute Zagreb, Federal Geological Institute*, Belgrade.

Janots E., Engi M., Berger A., Allaz J., Schwarz J.O. & Spandler C. 2008: Prograde metamorphic sequence of REE minerals in pelitic rocks of the Central Alps: implications for allanite–monazite–xenotime phase relations from 250 to 610 °C. *Journal of Metamorphic Geology* 26, 509–526. https://doi.org/10.1111/j.1525-1314.2008.00774.x

Janoušek V., Farrow C.M. & Erban V. 2006: Interpretation of whole-rock geochemical data in igneous geochemistry: introducing Geochemical Data Toolkit (GCDkit). *Journal of Petrology* 47, 1255–1259. https://doi.org/10.1093/petrology/egl013

Jefferies N.L. 1985: The distribution of the rare earth elements within the Carnmenellis pluton, Cornwall. *Mineralogical Magazine* 49, 495–504.

Kato T. 2005: New Accurate Bence-Albee α-Factors for Oxides and Silicates Calculated from the PAP Correction Procedure. *Geostandards and Geoanalytical Research* 29, 83–94. https://doi.org/10.1111/j.1751-908X.2005.tb00657.x

Krenn E., Schulz B. & Finger F. 2012: Three generations of monazite in Austroalpine basement rocks to the south of the Tauern Window: Evidence for Variscan, Permian and Eo-Alpine metamorphic events. *Swiss Journal of Geosciences* 105, 343–360. https://doi.org/10.1007/s00015-012-0104-6

Kretz R. 1983: Symbols for rock forming minerals. *American Mineralogist* 68, 277–279.

Ludwig K.R. 2004: Users manual for ISOPLOT/EX, version3.1. A geochronological toolkit for Microsoft Excel. *Berkeley Geochronology Center, Special Publication* 4.

Lumpkin G.R. & Chakoumakos B.C. 1988: Chemistry and radiation effects of thorite-group minerals from the Harding Pegmatite, Taos County, New Mexico. *American Mineralogist* 73, 1405–1419.

Mahan K.H., Goncalves P., Williams M.L. & Jercinovic M.J. 2006: Dating metamorphic reactions and fluid flow: application to exhumation of high-P granulites in a crustal-scale shear zone, western Canadian Shield. *Journal of Metamorphic Geology* 24, 193–217. https://doi.org/10.1111/j.1525-1314.2006.00633.x

Mielke P. & Winkler H.G.F. 1979: Eine bessere Berechnung der Mesonorm für granitische Gesteine. *Neues Jahrbuch für Mineralogie, Monatshefte* 10, 471–480.

Montel J.-M., Kato T., Enami M., Cocherie A., Finger F., Williams M. & Jercinovic M. 2018: Electron-microprobe dating of monazite: The story. *Chemical Geology* 484, 4–15. https://doi.org/10.1016/j.chemgeo.2017.11.001

Mottram C.M., Parrish R.R., Regis D., Warren C.J., Argles T.W., _ Harris N.B.W. & Roberts N.M.W. 2015: Using U–Th–Pb petrochronology to determine rates of ductile thrusting: Time windows into the Main Central Thrust, Sikkim Himalaya. *Tectonics* 34, 1355–1374. https://doi.org/10.1002/2014TC003743

Oelkers E.H. & Poitrasson F. 2002: An experimental study of the dissolution stoichiometry and rates of a natural monazite as a function of temperature from 50 to 230 °C and pH from 1.5 to 10. *Chemical Geology* 191, 73–87. https://doi.org/10.1016/S0009-2541(02)00149-3

Ondrejka M., Uher P., Putiš M., Broska I., Bačík P., Konečný P. & Schmiedt I. 2012: Two-stage breakdown of monazite by post-magmatic and metamorphic fluids: An example from the Veporic orthogneiss, Western Carpathians, Slovakia. *Lithos* 142, 245–255. https://doi.org/10.1016/j.lithos.2012.03.012

Pamić J. & Lanphere M. 1991: Hercynian Granites and Metamorphic Rocks from The Mts. Papuk, Psunj, Krndija, and The Surrounding Basement of The Pannonian Basin in Slavonija (Northern Croatia, Yugoslavia). *Geologija* 34, 81–253. https://doi.org/10.5474/geologija.1991.004

Pamić J., Lanphere M. & McKee E. 1988: Radiometric ages of metamorphic and associated igneous rocks of the Slavonian Mountains in the southern part of the Pannonian Basin, Yugoslavia: *Acta Geologica* 18, 13–39.

Pamić J., Balen D. & Tibljaš D. 2002: Petrology and geochemistry of orthoamphibolites from the Variscan metamorphic sequences of the South Tisia in Croatia–an overview with geodynamic implications. *International Journal of Earth Sciences* 91, 787–798. https://doi.org/10.1007/s00531-002-0258-y

Paton C., Woodhead J.D., Hellstrom J.C., Hergt J.M., Greig A. & Maas R. 2010: Improved laser ablation U-Pb zircon geochronology through robust downhole fractionation correction. *Geochemistry, Geophysics, Geosystems* 11. https://doi.org/10.1029/2009GC002618

Paton C., Hellstrom J., Paul B., Woodhead J. & Hergt J. 2011: Iolite: Freeware for the visualisation and processing of mass spectrometric data. *Journal of Analytical Atomic Spectrometry* 26, 2508–2518. https://doi.org/10.1039/C1JA10172B

Peterman E.M., Mattinson J.M. & Hacker B.R. 2012: Multi-step TIMS and CA-TIMS monazite U–Pb geochronology. *Chemical Geology* 312, 58–73. https://doi.org/10.1016/j.chemgeo.2012.04.006

Poitrasson F., Chenery S. & Bland D.J. 1996: Contrasted monazite hydrothermal alteration mechanisms and their geochemical implications. *Earth and Planetary Science Letters* 145, 79–96. https://doi.org/10.1016/S0012-821X(96)00193-8

Poitrasson F., Chenery S. & Shepherd T.J. 2000: Electron microprobe and LA-ICP-MS study of monazite hydrothermal alteration: Implications for U–Th–Pb geochronology and nuclear ceramics. *Geochimica et Cosmochimica Acta* 64, 3283–3297. https://doi.org/10.1016/S0016-7037(00)00433-6

Procházka V., Seydoux-Guillaume A.-M., Trojek T., Goliáš V., Korbelová Z., Matějka D. & Novotná P. 2011: Alteration halos around radioactive minerals in plutonic and metamorphic rocks of the northern Moldanubian area, Bohemian massif. *European Journal of Mineralogy* 23, 551–566. https://doi.org/10.1127/0935-1221/2011/0023-2108

Putnis A. & Putnis C.V. 2007: The mechanism of reequilibration of solids in the presence of a fluid phase. *Journal of Solid State Chemistry* 180, 1783–1786. https://doi.org/10.1016/j.jssc.2007.03.023

Santitharangkun S., Skrzypek E., Hauzenberger C.A., Gonzalez de Vega R. & Clases D. 2025: Deciphering multiple orogenic phases with the reactive help of monazite (Inthanon core complex, N Thailand). *Chemical Geology* 689, 122843. https://doi.org/10.1016/j.chemgeo.2025.122843

Schmid S.M., Bernoulli D., Fügenschuh B., Matenco L., Schefer S., Schuster R., Tischler M. & Ustaszewski K. 2008: The Alpine–Carpathian–Dinaridic orogenic system: correlation and evolution of tectonic units. *Swiss Journal of Geosciences* 101, 139–183. https://doi.org/10.1007/s00015-008-1247-3

Schneider P., Balen D., Opitz J. & Massonne H.-J. 2022: Dating and geochemistry of zircon and apatite from rhyolite at the UNESCO geosite Rupnica (Mt. Papuk, northern Croatia) and the relationship to the Sava Zone. *Geologia Croatica* 75. https://doi.org/10.4154/gc.2022.19

Schneider P., Gallhofer D., Skrzypek E., Hauzenberger C. & Balen D. 2025: Age and origin of a brief Late Cretaceous magmatic pulse based on geochemical data from accessory zircon (Mt. Papuk, Croatia). *Geologica Carpathica* 76. https://doi.org/10.31577/GeolCarp.2025.13

Schulz B. 2017: Polymetamorphism in garnet micaschists of the Saualpe Eclogite Unit (Eastern Alps, Austria), resolved by automated SEM methods and EMP–Th–U–Pb monazite dating. *Journal of Metamorphic Geology* 35, 141–163. https://doi.org/10.1111/jmg.12224

Schulz B. 2021: Monazite Microstructures and Their Interpretation in Petrochronology. *Frontiers in Earth Science* 9, 668566. https://doi.org/10.3389/feart.2021.668566

Schulz B., Brätz H., Bombach K. & Krenn E. 2007: In situ Th–Pb dating of monazite by 266 nm laser ablation and ICP-MS with a single collector, and its control by EMP analysis. *Zeitschrift für Geologische Wissenschaften* 35, 377–392.

Seydoux-Guillaume A.-M., Paquette J.-L., Wiedenbeck M., Montel J.-M. & Heinrich W. 2002: Experimental resetting of the U–Th–Pb systems in monazite. *Chemical Geology* 191, 165–181. https://doi.org/10.1016/S0009-2541(02)00155-9

Skrzypek E., Kawakami T., Hirajima T., Sakata S., Hirata T. & Ikeda T. 2016: Revisiting the high temperature metamorphic field gradient of the Ryoke Belt (SW Japan): New constraints from the Iwakuni-Yanai area. *Lithos* 260, 9–27. https://doi.org/10.1016/j.lithos.2016.04.025

Skrzypek E., Sakata S. & Sorger D. 2020: Alteration of magmatic monazite in granitoids from the Ryoke belt (SW Japan): processes and consequences. *American Mineralogist* 105, 538–554. https://doi.org/10.2138/am-2020-7025

Stacey J.T. & Kramers J. 1975: Approximation of terrestrial lead isotope evolution by a two-stage model. *Earth and Planetary Science Letters* 26, 207–221. https://doi.org/10.1016/0012-821X(75)90088-6

Stachowicz M., Bagiński B., Harlov D.E., Jokubauskas P., Matyszczak W., Kotowski J. & Macdonald R. 2024: Experimental synthesis of ThSiO4 by fluid-induced alteration of chevkinite-(Ce): Evidence for element mobility and variable crystal structure. *Chemical Geology* 670, 122429. https://doi.org/10.1016/j.chemgeo.2024.122429

Stepanov A.S., Hermann J., Rubatto D. & Rapp R.P. 2012: Experimental study of monazite/melt partitioning with implications for the REE, Th and U geochemistry of crustal rocks. *Chemical Geology* 300–301, 200–220. https://doi.org/10.1016/j.chemgeo.2012.01.007

Townsend K.J., Miller C.F., D'Andrea J.L., Ayers J.C., Harrison T.M. & Coath C.D. 2001: Low temperature replacement of monazite in the Ireteba granite, Southern Nevada: Geochronological implications. *Chemical Geology* 172, 95–112. https://doi.org/10.1016/S0009-2541(00)00238-2

Ustaszewski K., Kounov A., Schmid S.M., Schaltegger U., Krenn E., Frank W. & Fügenschuh B. 2010: Evolution of the Adria-Europe plate boundary in the northern Dinarides: From continent-continent collision to back-arc extension. *Tectonics* 29. https://doi.org/10.1029/2010TC002668

Williams M.A., Kelsey D.E. & Rubatto D. 2022: Thorium zoning in monazite: A case study from the Ivrea–Verbano zone, NW Italy. *Journal of Metamorphic Geology* 40, 1015–1042. https://doi.org/10.1111/jmg.12656

Williams M.L., Jercinovic M.J., Harlov D.E., Budzyń B. & Hetherington C.J. 2011: Resetting monazite ages during fluid-related alteration. *Chemical Geology* 283, 218–225. https://doi.org/10.1016/j.chemgeo.2011.01.019

Electronic supplementary material is available online:
Supplementary Table S1 at https://geologicacarpathica.com/data/files/supplements/GC-76-Skrzypek_TableS1.xlsx
Supplementary Table S2 at https://geologicacarpathica.com/data/files/supplements/GC-76-Skrzypek_TableS2.xlsx
Supplementary Table S3 at https://geologicacarpathica.com/data/files/supplements/GC-76-Skrzypek_TableS3.xlsx